Large eddy simulation of effects of oxidizer inlet temperatures on the transition routes before and after thermoacoustic instability in a subcritical hydrogen peroxide/kerosene liquid rocket engine ⊘

Yuanzhe Liu (刘远哲) ⓘ ; Peijin Liu (刘佩进) ⓘ ; Zhuopu Wang (王琢璞) ✉ ⓘ ; Wen Ao (敖文); Yu Guan (关昱) ⓘ

Check for updates

View Online   Export Citation

Articles You May Be Interested In

AIP Publishing

Physics of Fluids

Special Topics Open for Submissions

Learn More

AIP Publishing

Large eddy simulation of effects of oxidizer inlet temperatures on the transition routes before and after thermoacoustic instability in a subcritical hydrogen peroxide/kerosene liquid rocket engine

Yuanzhe Liu (刘远哲),[1] [iD] Peijin Liu (刘佩进),[1] [iD] Zhuopu Wang (王琢璞),[1,a] [iD] Wen Ao (敖文),[1] and Yu Guan (关昱)[2] [iD]

AFFILIATIONS

[1]Science and Technology on Combustion, Internal Flow and Thermal-structure Laboratory, Northwestern Polytechnical University, Xi'an 710072, China
[2]Department of Aeronautical and Aviation Engineering, The Hong Kong Polytechnic University, Kowloon, Hong Kong

[a]Author to whom correspondence should be addressed: zpwang@nwpu.edu.cn

ABSTRACT

This paper presents the first numerical evidence of the intermittency routes that exist before and after the occurrence of thermoacoustic instability in a subcritical single-element liquid rocket engine burning liquid kerosene and decomposed hydrogen peroxide with increasing oxidizer inlet temperatures (T). Three-dimensional compressible large eddy simulation algorithms, combined with Euler–Lagrangian frameworks, are employed to model the spray turbulent combustion process in a high-pressure rocket combustor where a one-equation eddy viscosity sub-grid turbulence model and a PaSR sub-grid combustion model are used based on OpenFOAM. After verifying the numerical framework and achieving grid independence, we focus on (i) dynamical transition routes before and after the thermoacoustic regime, (ii) frequency-locking phenomena between acoustic perturbations, vortex dynamics, and combustion heat release, and (iii) the underlying physical mechanisms associated with different dynamical states. The results show that as we increase the oxidizer inlet temperature ($700 \, \text{K} \leq \text{T} \leq 900 \, \text{K}$), the system dynamics undergo a transition from a state of combustion noise to a period-1 limit cycle via intermittency. Furthermore, by further increasing the oxidizer inlet temperature ($950 \, \text{K} \leq \text{T} \leq 1450 \, \text{K}$), a second bifurcation occurs, causing a transition from a limit cycle state back to a combustion noise state also via intermittency. These bifurcation phenomena are attributed to frequency-locking interactions among pressure fluctuations, combustion heat release, and vortex dynamics. Evidence from combustion flow subsystems including mixture fraction, burning modes, and flame-induced vorticity sources provides additional insights into the complex instability mechanism.

Published under an exclusive license by AIP Publishing. https://doi.org/10.1063/5.0177903

I. INTRODUCTION

The phenomenon of combustion instability (CI) observed in liquid rocket engines (LREs) has posed a formidable challenge in recent decades.[1–4] Combustion instability, known as thermoacoustic instability, manifests as high-amplitude pressure oscillations resulting from a positive feedback loop involving unsteady combustion, hydrodynamic instability, and acoustics.[5–7] The significant amplitude oscillations can also result in enhanced heat transfer, thereby augmenting the efficiency of mass, momentum, and energy transport within the combustion chamber and modifying the engine's thrust level from its original design specifications.[8] Even low-amplitude vibrations can lead to fatigue-induced mechanical component failure. The presence of high-amplitude pressure oscillations poses a significant risk of severe

damage to combustor components, including liner tubes and fuel injectors. Therefore, it is imperative to identify thermoacoustic instability during the design phase of rocket engines.[9]

A. CI in coaxial LREs

Lord Rayleigh was the first to propose a scientific explanation for the emergence of thermoacoustic instability: When there is a phase synchronization between heat release and pressure signal, it leads to energy transfer from the combustion field into the acoustic field, thereby amplifying oscillations.[10] A system is considered linearly unstable when it can spontaneously exhibit thermoacoustic instability without any artificial perturbation. Conversely, a system is deemed linearly stable if it maintains a state of combustion noise under conditions

that are not artificially perturbed.[11] However, even a linearly stable system can become unstable when subjected to an external perturbation of finite amplitude, which is referred to as triggering thermoacoustic instability or nonlinear instability.[12] Combustion instability encompasses various sub-processes of combustion flow, with a more comprehensive understanding achieved regarding the confinement's acoustic propagation. However, there remains incomplete knowledge concerning the coupling mechanisms among fluid dynamics, acoustics, and flame dynamics. The occurrence of combustion instability in liquid rocket engines is closely associated with specific configurations or operating conditions, yet a comprehensive mechanism has not been identified thus far.[9] This paper aims to investigate the phenomenon of combustion instability and clarify its underlying physical mechanisms in a single-element coaxial liquid rocket combustor with a gas-phase oxidizer-centered and liquid fuel-swirled injector. In coaxial liquid rocket engines with gas-centered injectors, periodic vortex shedding occurs downstream of the injector plane.[13] The flame is stabilized by regions characterized by high-velocity gradients, such as shear layers. In such configurations, the interaction between the flame and vortices serves as the primary driving mechanism for combustion instability. When combustion instability occurs, hydrodynamic, acoustic, and combustion feedback loops are formed, resulting in a matching of the vortex shedding frequency with the acoustic frequency.[14]

1. Experimental efforts

Over the past two decades, extensive experimental efforts have been dedicated to investigating combustion instability in coaxial liquid rocket engines. The most representative teams conducting these experiments are DLR Lampoldshausen in Germany[15] and William Anderson[16] at Purdue University. In recent years, the primary focus of DLR's research on combustion instability has revolved around two test instruments: BKH and BKD. BKH[17,18] employs an external mechanical device to induce acoustic excitation in the combustion chamber, enabling the study of the coaxial jet unit's response to acoustic disturbances. Additionally, a high-frequency pressure sensor is utilized to record pressure signals. By means of shadow imaging technology, the deformation of the liquid oxygen jet and flame response of the coaxial jet unit are observed through an optical window situated on the side of the combustion chamber using a high-speed camera. The shadow image obtained from BKH reveals that under transverse velocity perturbation conditions, transverse instability accelerates both breaking and mixing processes within liquid oxygen, resulting in a reduction in its penetration length. Simultaneously, OH* chemiluminescence imaging demonstrates corresponding changes in flame range, luminescence intensity, and flame dynamics. The BKD is utilized as a testing apparatus to investigate the instability of self-excited combustion.[19,20] It consists of a sub-scale rocket engine equipped with 42 coaxial injection elements. The propellant used in this system is LOx/H$_2$, and it operates under supercritical conditions. Groning et al.[21] employed high-frequency pressure sensors and optical probes within the combustion chambers to examine high-frequency combustion instability. In the case of the BKD combustion chamber, fluctuations in the OH* intensity observed by the optical probe exhibit a dominant frequency that aligns with the acoustic resonance frequency of the LOx post, regardless of acoustic characteristics of the combustion chamber itself. When one of the resonant frequencies of the LOx post coincides with its first

transverse (1T) frequency, 1T mode instability occurs within this configuration.

Two experimental setups were operated at Purdue University: the Continuously Variable Resonant Chamber (CVRC),[22] which is a single-element liquid rocket engine, and the Transverse Instability Combustor (TIC),[23] used for analyzing spontaneous transverse combustion instability. The CVRC combines a combustor with a coaxial oxidizer gas-centered injector that burns dissociated hydrogen peroxide as the oxidizer and liquid kerosene[24] or gaseous methane[16] as the fuel. It focuses on different stability regimes due to variations in the length of either the oxidizer post or the combustion chamber.

2. The status of numerical simulation

Despite the considerable amount of exceptional experimental work conducted, the fundamental physical mechanisms underlying the emergence of combustion instability remain a central issue in the rocket community due to a dearth of adequate experimental observational techniques in high-temperature and high-pressure environments, particularly concerning combustion visualization. To tackle this challenge, computational fluid dynamics (CFD) methods have been extensively employed for investigating thermoacoustic instability. In recent years, large eddy simulations (LES), as an exemplary representative of high-fidelity simulations, have increasingly been utilized for engineering purposes and parametric studies.[9] The triggering of a transverse thermoacoustic instability in a supercritical BKD combustor at different equivalence ratios was investigated using compressible LES algorithms by Urbano et al.[25] The self-excited transverse instability of a multi-element rectangular model rocket motor was similarly investigated using LES by Guo et al.[26] Transverse combustion instability was previously regarded as highly destructive and received significant attention. However, in recent years, longitudinal instability has gained prominence during the development of high-thrust coaxial liquid rocket engines due to its potential coupling with the injection system. Numerous studies at CVRC have numerically investigated the impact of various acoustic resonance conditions on self-excited longitudinal thermoacoustic instability. In numerical firing tests burning gaseous methane, control parameters such as the length of the oxidizer post[27] and combustion chamber,[28] as well as the wall temperature of the combustor,[29] are altered to observe different stability regions. However, there remains a scarcity of studies investigating the longitudinal thermoacoustic instability associated with the subcritical spray combustion process in coaxial single-element liquid-fueled rocket engines. The interaction between the gas and liquid phases gives rise to intricate coupling mechanisms for thermoacoustic instability. Therefore, in this study, a LES algorithm, combined with Euler–Lagrangian frameworks, is used to analyze the thermoacoustic instability in a single-element coaxial liquid rocket engine and its underlying physical mechanism.

B. Dynamical system theory in CI

Another challenge in the rocket propulsion community is to identify the dynamical transition route from stable operation to thermoacoustic instability due to changes in control parameters. Introducing terminology from dynamical systems theory, the traditional view suggests that the system dynamics transition from the state of combustion noise to thermoacoustic instability occurs via a Hopf

bifurcation, which is a direct transition from a fixed point (FP) to a limit cycle state.[2,3] The limit cycle state represents an oscillation with constant amplitude and frequency. However, over the past decade, nonlinear time series analysis has provided increasing evidence of complex pressure oscillations beyond the limit cycle and fixed point in various thermoacoustic systems, including quasi-periodic oscillations,[30] intermittency,[31] chaos,[32] and period-n oscillations.[33] For high Reynolds number and high energy density combustors such as liquid rocket engines, intermittency presages the occurrence of thermoacoustic instability as demonstrated by Aoki *et al.*[34] and Kasthuri *et al.*[35] By systematically varying the control parameters, they observed that the onset of thermoacoustic oscillations was always preceded by intermittent bursts of high-amplitude periodic oscillations that appeared in a nearly random manner in the region of low-amplitude non-periodic fluctuations. As the operating conditions approach the thermoacoustic instability regime, the duration of these periodic oscillations continues for a longer period until the system fully transitions to a state of periodic oscillations.[34] The traditional paradigm of thermoacoustic instability involves a transition from stable operation (fixed point) to unstable operation (limit cycle point). An alternative transition paradigm proposed by Sujith and co-workers suggests stable operation $\rightarrow$ intermittency $\rightarrow$ thermoacoustic instability.[2,35–37] The emergence of thermoacoustic instability involves synchronization processes between various subsystems of the combustion flow fields,[14,38] which means that simultaneous examination between multiple subsystems under different nonlinear states is necessary. A weighted spatial network analysis of local flame intensity oscillations during the transition from intermittency to thermoacoustic instability in a TIC combustor was performed by Kasthuri *et al.*[39] Kasthuri *et al.*[40] also investigated the coupled interaction of pressure oscillations and localized CH* chemiluminescence oscillation strengths during the transition to thermoacoustic instability in the TIC combustor.

C. The main contributions of the present study

Although previous work has shed some light on the intermittency before thermoacoustic instability in model liquid rocket engines, it is far from complete. The simultaneous examination of combustion flow field subsystems associated with the transition route from a combustion noise state to a thermoacoustic state due to changes in control parameters continues to fascinate researchers. On the other hand, it has been found in several thermoacoustic systems that, in addition to the intermittency that precedes the thermoacoustic instability, as the control parameter continues to increase, the system undergoes a secondary bifurcation, which may lead to more complex nonlinear states rather than just period-1 oscillations.[1] However, research on the secondary bifurcation phenomenon in liquid rocket engines is still lacking. Meanwhile, to the best of our knowledge, most of the current reports on intermittency in liquid rocket engines focus on gas-phase propellants such as turbulent combustion of gas-oxygen/methane (GO_2/GCH_4)[35,39,40] or gas-oxygen/hydrogen (GO_2/H_2)[14,34,38] under subcritical conditions. The working conditions of liquid rocket engines often involve high-pressure environments, with the combustion chamber operating within a pressure range of 1 MPa to over 20 MPa. Considering that the operating pressure of upper stage engines typically falls below the critical pressure of fuel and oxidizer, it remains essential to investigate spray combustion stability under subcritical conditions. This study primarily focuses on examining the combustion

stability of hydrogen peroxide/kerosene rocket engines in subcritical scenarios. In our previous paper in 2023,[41] using the LES approach, we discussed the existence of an intermittency route ($1.3 \leq \phi \leq 0.9$) to period-2 instability ($\phi = 0.7, 0.5$) after period-1 oscillations ($\phi = 1.5$) in a subcritical hydrogen peroxide/kerosene single-element liquid-fueled rocket engine, as we decrease the equivalence ratio (ϕ) from fuel-rich condition to fuel-lean condition ($1.5 \leq \phi \leq 0.5$). The large eddy simulation algorithm offers distinct advantages over experimental measurements in obtaining additional data on combustion flow subsystems, as it is not constrained by combustion diagnostic measures. This allows for an investigation into the synchronization process between multiple subsystems at the onset of thermoacoustic instability. Therefore, in this paper, we continue to employ the large eddy simulation algorithm as a research strategy. Additionally, the Euler–Lagrange framework is utilized to handle the interaction between gas and liquid phases in spray combustion, neglecting the atomization process and treating discrete droplets as Lagrangian parcels while modeling the gas phase using the Euler method. The thermoacoustic instability of rocket engines can be categorized into longitudinal and transverse instabilities. Since the occurrence of transverse instability in the F-1 engine,[42] researchers have increasingly focused on investigating the mechanism of transverse thermoacoustic instability and corresponding suppression measures, such as incorporating baffles.[43] However, in recent years, with the advancement of coaxial liquid rocket engines, the issue of longitudinal thermoacoustic instability has become more prevalent due to the interaction between the injection element and combustion chamber. Regrettably, conventional engineering approaches like baffles have proven ineffective in addressing this problem. Consequently, replacing transverse instability with longitudinal thermoacoustic instability has emerged as a new challenge in liquid rocket engine community. Longitudinal thermoacoustic instability takes precedence in this study, replacing transverse instability as a critical concern in full-size liquid rocket engines. To ensure computational affordability without compromising realism, a single-element coaxial liquid rocket engine operating under real rocket conditions serves as our computational configuration.

The first objective of this study is to investigate the presence of intermittent behavior preceding the thermoacoustic instability region, as well as to examine the associated lock-in phenomenon in the subsystem of turbulent spray combustion flow field. The control parameter chosen for this investigation is the oxidizer inlet temperature, which influences flame stability by altering the density ratio between unburnt reactants and combustion products.[44] Moreover, in subcritical spray combustion flow fields, variations in oxidizer inlet temperature also impact liquid fuel evaporation rate; specifically, higher oxidizer inlet temperatures result in shorter evaporation distances. In a real rocket engine, the reactants are generally preheated into the combustion chamber. The engine simulated in this paper employs a two-component propellant, which is dissociated hydrogen peroxide at high temperature as the oxidizer and liquid kerosene at room temperature as the fuel. According to the CVRC experimental conditions,[27,45,46] the oxidizer comprises a mixture of 90% hydrogen peroxide and 10% water, which undergoes complete dissociation at 1030 K into 42% oxygen and 58% water vapor (per unit mass), with both oxygen and water existing in the gaseous phase under standard conditions. Therefore, the preheating temperature of the oxidizer is a critical parameter for real engine conditions, as it can significantly change the

09 January 2025 08:14:45

combustion stability. Currently, the investigation of the impact of reactant temperature on combustion stability primarily focuses on the gas turbine community.[44,47,48] Unni and Sujith[36] demonstrated that augmenting the reactant temperature results in enhanced combustion instability. In our recently published paper, we illustrate that within a single-element liquid rocket engine utilizing methane gas and hydrogen peroxide as propellants, there exist intermittency routes preceding and following the thermoacoustic instability regime within the parameter space of oxidizer inlet temperature.[49] Consequently, it raises a pertinent query regarding whether analogous principles are applicable to more intricate subcritical turbulent spray rocket combustor. Regrettably, there is currently no published literature documenting the transition from stable operation to thermoacoustic instability within the parameter space of preheated reactant temperatures for turbulent spray flames. The second purpose of this paper is to continue to explore whether a second bifurcation in the system dynamics occurs as we continue to increase the oxidizer inlet temperature and whether the appearance of a second bifurcation causes the system dynamics to change from a thermoacoustic unstable state toward some other nonlinear state. The third objective of this paper is to identify evidence that makes the thermoacoustic system dynamics change from the perspective of the combustion flow field. To this end, we examine the mixture fraction and the flame index to provide further insight into the flame dynamics at different dynamical states before and after thermoacoustic instability. Various terms in the vorticity transport equation are also examined, involving the vortex stretching term, the vortex dilatation term, and the baroclinic torque term. In conclusion, this paper provides a comprehensive study of the effect of oxidizer inlet temperature on the (i) dynamic transition route before and after thermoacoustic regime, (ii) corresponding frequency-locking routes between acoustic perturbations, vortex dynamics and combustion heat release, and (iii) underlying physical mechanisms leading to the transition of the system dynamics.

II. NUMERICAL FRAMEWORK

A. Governing equations and sub-grid models

In large eddy simulation, the full Navier–Stokes equations are filtered, with the large-scale flow being directly solved by the grid's filtered size and sub-grid turbulence models used to model smaller-scale flows. The three-dimensional complete filtered compressible Navier–Stokes equations include conservation equations for mass, momentum, and energy as well as species transport equations for calculating multi-component gas mixtures. The Euler–Lagrangian framework is utilized to describe the interaction between gas and liquid. In this framework, the liquid phase is represented as a Lagrangian particle, while the gas phase is described using the Eulerian method. In this paper, neither the dynamics of fuel droplets through injectors nor atomization processes in combustion chambers are directly modeled; instead, they are represented by a fixed Rosin–Rammler droplet size distribution. In LES of spray turbulent reactive flow, the flow variable $f(x, t)$ can be decomposed as $f(x, t) = \overline{f}(x, t) + \widetilde{f}(x, t)$, where $\overline{f}(x, t)$ is the low-pass filter variable and $\widetilde{f}(x, t)$ is the sub-grid variable. The mathematical expressions are as follows:

$$\frac{\partial \overline{\rho}}{\partial t} + \frac{\partial \overline{\rho} \widetilde{u}_j}{\partial x_j} = \overline{\overline{S}}_{mass}, \quad (1)$$

$$\frac{\partial \overline{\rho} \widetilde{u}_j}{\partial t} + \frac{\partial (\overline{\rho} \widetilde{u}_i \widetilde{u}_j)}{\partial x_i} + \frac{\partial \overline{p}}{\partial x_j} = \frac{\partial (\overline{\tau}_{ij} - \overline{\rho}(\widetilde{u_i u_j} - \widetilde{u}_i \widetilde{u}_j))}{\partial x_i} + \overline{\overline{S}}_{momentum}, \quad (2)$$

$$\frac{\partial \overline{\rho} \widetilde{h}_s}{\partial t} + \frac{\partial (\overline{\rho} \widetilde{u}_i \widetilde{h}_s)}{\partial x_i} = = \frac{\overline{Dp}}{Dt} + \frac{\partial}{\partial x_i} \left[\lambda \frac{\partial T}{\partial x_i} - \overline{\rho} (\widetilde{u_i h_s} - \widetilde{u}_i \widetilde{h}_s) \right]$$
$$+ \overline{\tau_{ij} \frac{\partial u_i}{\partial x_j}} - \frac{\partial}{\partial x_i} \left(\overline{\rho \sum_{k=1}^{N} V_{k,i} Y_k h_{s,k}} \right) + \overline{\overline{S}}_{energy}, \quad (3)$$

$$\frac{\partial (\overline{\rho} \widetilde{Y}_k)}{\partial t} + \frac{\partial (\overline{\rho} \widetilde{u}_i \overline{Y}_k)}{\partial x_i} = \frac{\partial}{\partial x_i} \left[\overline{V_{k,i} Y_k} - \overline{\rho} (\widetilde{u_i Y_k} - \widetilde{u}_i \widetilde{Y}_k) \right] + \overline{\overline{S}}_{species}$$
$$k = 1, N, \quad (4)$$

where, ρ, u_j, p, h_s, Y_k are mass density, the j th velocity, pressure, enthalpy, and the k th mass fraction, respectively. τ_{ij} denotes the stress tensor. $\overline{\overline{S}}_{mass}$, $\overline{\overline{S}}_{momentum}$, $\overline{\overline{S}}_{energy}$, and $\overline{\overline{S}}_{species}$ denote source terms resulting from the interaction between gas and liquid phases, as well as chemical reactions. For the laminar diffusion fluxes effect $V_{k,i} Y_k$, the mathematical expression, based on the gradient assumption with the unitary Lewis number (Le = 1), is as follows:

$$\overline{V_{k,i} Y_k} = -\overline{\rho} D_k \frac{\partial_i \widetilde{Y}}{\partial x_i}. \quad (5)$$

The stress tensor τ_{ij} for a mixture of multiple species can be expressed as

$$\tau_{ij} = -\mu \left(\frac{\partial u_i}{\partial x_j} + \frac{\partial u_j}{\partial x_i} - \frac{2}{3} \delta_{ij} \frac{\partial u_k}{\partial x_k} \right) - \mu_t \left(\frac{\partial u_i}{\partial x_j} + \frac{\partial u_j}{\partial x_i} - \frac{2}{3} \delta_{ij} \frac{\partial u_k}{\partial x_k} \right) + \tau_{ij,r}, \quad (6)$$

where μ denotes the dynamic viscosity, μ_t denotes the turbulent viscosity, δ_{ij} denotes the Kronecker delta, and $\tau_{ij,r}$ denotes the Reynolds stress tensor.

In the filtered equations, modeling is required for terms related to the unsolved sub-grid scale. This paper utilizes a one-equation eddy viscosity model[50] as the sub-grid turbulence model. The PaSR (Partially Stirred Reactor) combustion model was employed to account for the interaction between turbulence and finite rate chemical reactions, which has been shown in recent literature to provide convincing simulations of both premixed and non-premixed flames.[41,51–53] In this paper, the empirical parameters in the PaSR turbulent combustion model take the predefined values in OpenFOAM, that is, $C_{mix} = 0.15$. The liquid fuel undergoes successive atomization and evaporation processes during injection into the combustion chamber from the injector, as well as turbulent mixing with the gaseous oxidizer and subsequent combustion. These complex physicochemical sub-processes require corresponding atomization sub-models, evaporation models, heat transfer models between liquid and gas phases, droplet-wall interaction models, drag force models for droplets, etc. Therefore, Table I details the corresponding sub-models used in this paper. For a more detailed mathematical description, the reader is referred to literature.[50,54]

B. Physical models and boundary conditions

The computational configuration examined in this paper is based on a laboratory-scale liquid rocket engine designed at Purdue

TABLE I. Spray sub-models.

Model	Name
Injection	Cone nozzle injection
Composition	Single phase mixture
Atomization	None
Breakup	ReitzKHRT
Evaporation	Liquid evaporation boil
Heat transfer	RanzMarshall
Wall interaction	Rebound
Drag force	Sphere

University burning kerosene and hydrogen peroxide.[45,55] The experimental setup featured a gas-centered, liquid-swirled coaxial injector, a combustion chamber, and a short nozzle, as depicted in Fig. 1(a). Liquid kerosene enters the combustion chamber in a swirling flow centered on the oxidizer. At this point, the fuel's atomization process is not taken into account, and it is injected as a cone manner with a fixed Rosin-Rammler droplet size distribution. The oxidizer is a mixture of 90% hydrogen peroxide and 10% water, which dissociates completely into 42% oxygen and 58% water vapor (per unit mass) before entering the combustion chamber. The oxidizer is injected into the combustion chamber at 1030 K, where both oxygen and water are in the gaseous phase (under standard experimental conditions).

The length of the combustion chamber was 38.1 cm, and the diameter was 4.5 cm, while the oxidizer post had a length of 17 cm and a diameter of 2.05 cm. The end of the combustion chamber is connected to an acoustically choked short nozzle where the flow reaches supersonic speeds. The throat diameter of the nozzle is 2.1 cm. To ensure the orthogonality of mesh, three-dimensional block-structured hexahedral grids were generated. In Sec. III A, we examine the sensitivity of computational results for three alternative mesh resolutions, containing 2.1×10^6, 4.2×10^6, and 6.1×10^6 hexahedral cells. Figures 1(b) and 1(c) show a medium-structured hexahedral grid near the dump plane and the nozzle.

Three monitoring points were set up, as shown in Fig. 2, to quantitatively monitor the time evolution of the combustion flow field. These points are called probe 1 (1, 2.2, 0 cm), probe 2 (1, 1, 0 cm), and probe 3 (6, 1, 0 cm). Probe 1 was located near the wall of the
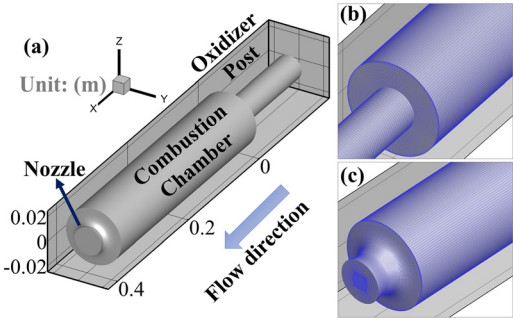

FIG. 1. (a) Schematic of the three-dimensional computational domain. (b) The local mesh near the dump plane ($x = 0$). (c) The local mesh near the nozzle.
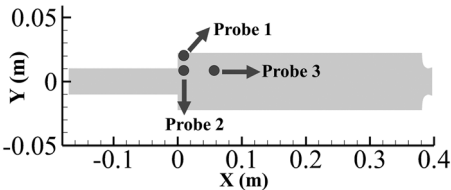

FIG. 2. Slice of the two-dimensional view (x-y plane) and labeled monitoring points.

combustion chamber and close to the antinode of the first-order acoustic mode of the combustion chamber to monitor pressure time series. Local velocities and heat release rates (HRRs) were monitored at probes 2 and 3, which were located in the shear layer where fuel and oxidant mix and combust. As the fluid passes through the dump plane, vortices form and are convected downward, passing successively through probes 2 and 3. In particular, probe 2 was positioned at the initial shear layer, coinciding with the passage of the vortex core (at $x/D_{outer} = 0.43$, where x represents the axial distance from the dump plane and D_{outer} denotes the diameter of jet). The frequency associated with the highest peak in velocity spectrum at this location can be identified as the frequency of vortex shedding, a widely utilized concept in existing literature.[56–58] The monitoring point probe 3 was set to further investigate the response of flame and vortex dynamics at different spatial locations.

The specific boundary conditions and parameter settings are presented in Table II. At the inlet of the oxidizer, constant mass flow rate boundary conditions were imposed in conjunction with zero-gradient pressure boundary conditions, thus ensuring rigid acoustic boundary conditions. The turbulent Intensity Kinetic Energy Inlet boundary conditions were implemented at the fuel/oxidizer inlet, where the turbulent kinetic energy values were obtained through interpolation based on calculation results. The mass flow rate of the oxidizer was 0.231 kg/s, which contained 42% oxygen and 58% water vapor (per unit mass). The inlet temperature of the oxidizer is the main variable in this paper. During the experiment, it constantly changed in the range from 700 to 1450 K. Liquid kerosene was treated as discrete Lagrangian parcels with a mass flow rate of 0.037 kg/s at 300 K. The size distribution of

TABLE II. Calculation conditions.

Part	Boundary condition	Value
Oxidizer inlet	Mass flow rate	0.231 kg/s
	Temperature	$700 \leq T \leq 1450$ K
	Mass composition	42% O_2 + 58% H_2O
Fuel inlet	Mass flow rate	0.037 kg/s
	Rosin–Rammler distribution	$n = 3$
		$d_{32} = 50 \,\mu m$
	Cone angle	90°
	Parcels per seconds	20 000 000
	Temperature	300 K
	Mass composition	100% $C_{12}H_{26}$
Walls	No-slip; adiabatic; impermeable walls	
Outlet	Wave transmissive	0.5 MPa

TABLE III. Chemical kinetic mechanism.

Reaction	A (s^{-1})	Ea J/(kg mol)	b	c	d
$C_{12}H_{26} + 18.5O_2 \rightarrow 12CO_2 + H_2O$	5×10^8	15 780	0	0.25	1.5

the paraffin droplets was a Rosin–Rammler distribution, where the Sauter mean diameter $d_{32} = 50\,\mu m$ and the spread parameter $n = 3$. The number of parcels per second was set to 20×10^6. The experiment was conducted at a nominal mixture ratio (O/F) of approximately 6.3 and a nominal chamber pressure of around 1.2 MPa. All wall surfaces were treated as non-slip, impermeable, rigid acoustic boundaries as well as being adiabatic walls. The outlet was set as a wave transmissive boundary condition, due to the supersonic nature of the flow at the exit. This boundary condition ensured that no acoustic waves were reflected into the combustion chamber.

C. Numerical procedure

Three-dimensional large eddy simulations were performed based on the Euler–Lagrangia framework, which involves a gaseous phase, liquid phase, and the interaction between both, using the open-source CFD toolbox OpenFOAM with a modified version of sprayFoam. The Favre-averaged filtered Navier–Stokes equations were numerically solved for the gaseous phase, including mass, momentum, species transport, and energy equations (also known as the Euler approach). For the liquid phase, a Lagrangian approach was adopted for this study. To account for interactions between the gaseous and liquid phases, a two-way coupling approach was used by solving source terms with various spray sub-models. In LES, a one-equation eddy viscosity sub-grid turbulence model[50,59] combined with the PaSR sub-grid turbulent combustion model[60] was employed to simulate the turbulent spray combustion process. There is an empirical parameter, Ck = 0.07, in the sub-grid turbulence model.

In the rocket propulsion community, kerosene serves as a widely utilized hydrocarbon fuel. Due to its intricate composition, we exclusively employ n-dodecane ($C_{12}H_{26}$) as an alternative fuel in this study, owing to its extensive range of accessible chemical reaction mechanisms and the availability of experimental validation data.[50,61] The single-step global chemical reaction mechanism is considered here to balance computational accuracy and efficiency, which has already proven to be effective in simulating combustion instability in rocket engines.[28,41,55,62,63] The detailed chemical reaction mechanism and related parameters are shown in Table III.

The combustion chamber operated at a pressure of 1.2 MPa, which was below the critical pressure for kerosene, oxygen, and water. Therefore, the density of the gas phase mixture was calculated using the ideal gas equation of state, which has also been proven to be efficient in our previous study.[41] The gas mixture is assumed to be ideal and linearly viscous with Fickian diffusion and Fourier heat transfer. The laminar viscosity was modeled using Sutherland's law, while the specific heat of each species was calculated using JANAF thermochemical tables.

The code employs an unstructured collocated finite volume method (FVM) with discretization based on Gauss' theorem and a semi-implicit time-integration scheme. For pressure-velocity coupling, it uses the PIMPLE method, which is derived from the SIMPLE and PISO algorithms, making it suitable for transient simulations. The diffusion and convection terms were discretized using second-order central difference schemes, and time integration was performed using a first-order Euler scheme to improve calculation stability. An adjustable time step was employed to control the calculation time, with an upper limit of the CFL number set at 0.6. As a result, the calculated time step was 8×10^{-8} s. The present study employs approximately 36 000 CPU cores for each operating condition, with a processing frequency of around 2.4 GHz per individual CPU core.

III. RESULTS AND DISCUSSION

The numerical framework used in this paper was validated against experimental measurements contained in our previous paper in 2023.[41] Two different benchmark cases were employed: Spray A[64] was used to verify the interaction between the gas and liquid phases, while the self-excited thermoacoustic instability results of CVRC[55] were obtained from a single-element model rocket engine burning kerosene at critical pressure. A detailed comparison between the simulation results and the experimental results is presented in Appendix of this paper to maintain overall coherence.

A. Mesh details and validation

In this section, the effects of three different resolution grids on the computational results are investigated, aiming to identify the optimal grid configuration that strikes a balance between computational efficiency and accuracy. Three distinct hexahedral meshes based on a block structure were generated for a single-nozzle coaxial liquid rocket combustor, comprising 2×10^6, 4×10^6, and 6×10^6 hexahedral cells. The smallest mesh sizes were concentrated near the shear layer and combustor wall as indicated in Table IV. The tables present the distribution of grid nodes along both axial and cross-sectional directions for the oxidizer post and combustion chamber.

TABLE IV. Comparison of different three-dimensional grid resolutions.

Mesh	Oxidizer post Nodes	Length, mm Δx	$(\Delta r)min$	$(\Delta r)max$	Combustion chamber Nodes	Length (mm) Δx	$(\Delta r)min$	$(\Delta r)max$	Cells ($\times 10^6$)
1	$120 \times 42 \times 42$	1.4	0.2	1	$335 \times 66 \times 66$	1.14	0.06	1	2
2	$140 \times 42 \times 42$	1.2	0.2	1	$720 \times 66 \times 66$	0.5	0.06	1	4
3	$170 \times 42 \times 42$	1	0.2	1	$920 \times 73 \times 73$	0.4	0.06	1	6

The time series of pressures monitored at probe 1 were used to quantitatively compare the differences in LES results calculated between the three grids, as shown in Fig. 3. The delay time is determined based on the recommended value in the nonlinear dynamics textbook, which suggests using one quarter of the oscillation period. In the thermal-acoustic community, it is common to employ two-dimensional or three-dimensional embedded dimensions, a practice widely adopted in numerous previous studies.[35,65,66] The firing condition at the oxidizer inlet temperature of 900 K is considered here, as the LES results demonstrate that this condition is within the thermo-acoustic instability regime and is the main focus of this paper. All three cases show a time evolution of the pressure at high amplitudes, indicating the occurrence of a significant thermoacoustic instability. However, sharp peaks of different amplitudes are observed near the dominant frequency for these three cases, i.e., 0.085, 0.1126, and 0.1297 MPa. The results of mesh 2 are the closest to those of mesh 3 showing a tolerable error.

During combustion instability, in addition to high-amplitude pressure oscillations, the local velocities, temperatures, and the mass fraction of species in the combustion chamber have organized properties, which are manifested as periodic oscillations of multiple combustion flow subsystems. The velocity oscillations in the shear layer are the main indicator of global hydrodynamic instability and therefore serve as a second proof of mesh sensitivity. Figure 4 shows an overview of the dynamics of axial velocity monitored at probe 2. Similar to the dynamics of pressure signals, the systems of all three grids exhibit: (i) oscillations of high amplitude, (ii) sharp peaks near the first-order acoustic modes, and (iii) a single-loop structure in phase space. Qualitatively, the time series as well as the phase space of meshes 2 and 3 are highly similar, while the phase space structure of mesh 1 suggests multiple centers of rotation. Quantitatively, the first-order modes of mesh 1, mesh 2, and mesh 3 correspond to oscillation amplitudes of 37.3, 44.46, and 47.7 m/s, respectively, and thus the results of mesh 2

are in excellent agreement with those of the finest mesh 3. Considering the effect of computational efficiency, mesh 2 is used in subsequent calculations in this paper.

B. Effect of oxidizer inlet temperatures on cold flows

Prior to discussing combustion instability phenomena, we initially conducted a large eddy simulation (LES) of cold flows at varying oxidizer inlet temperatures, namely 750, 1050, and 1350 K. While chemical reactions were not considered, all other procedural settings remained consistent. This examination was focused on the intrinsic global hydrodynamic instability modes without accounting for flame-vortex dynamics interaction, serving as reference cases for subsequent thermoacoustic instability analysis.

Figures 5(a)–5(c) and 5(g)–5(i) illustrate the time series of local velocity perturbations and the corresponding fast Fourier transform (FFT) results for different oxidizer inlet temperatures: T = 750, 1050, and 1450 K monitored at probes 2 and 3. The axial velocity and y-direction velocity monitored at probe 2, located downstream of the dump plane in the initial shear layer, are presented for first comparison. The velocity perturbation is calculated as $u' = u - \overline{u}$, where $\overline{u}$ represents the average velocity. Both axial and y-direction velocities exhibit temporal variations across all three conditions due to flow separation between high-velocity and low-velocity streams downstream of the dump plane. Increasing the oxidizer inlet temperature enhances the global hydrodynamic pattern of the system, as evidenced by an increase in amplitude of velocity oscillations. However, no significant peak is observed in the FFT results of axial velocity at T = 750 K. In contrast, a slight amplitude peak appears near 7371 Hz in FFT results for y-directional velocity, while oscillations are suppressed between 0 and 5000 Hz. Comparing both directional signals suggests that radial velocity represents an intrinsic hydrodynamic instability, whereas axial velocity is more susceptible to acoustic interference resulting in
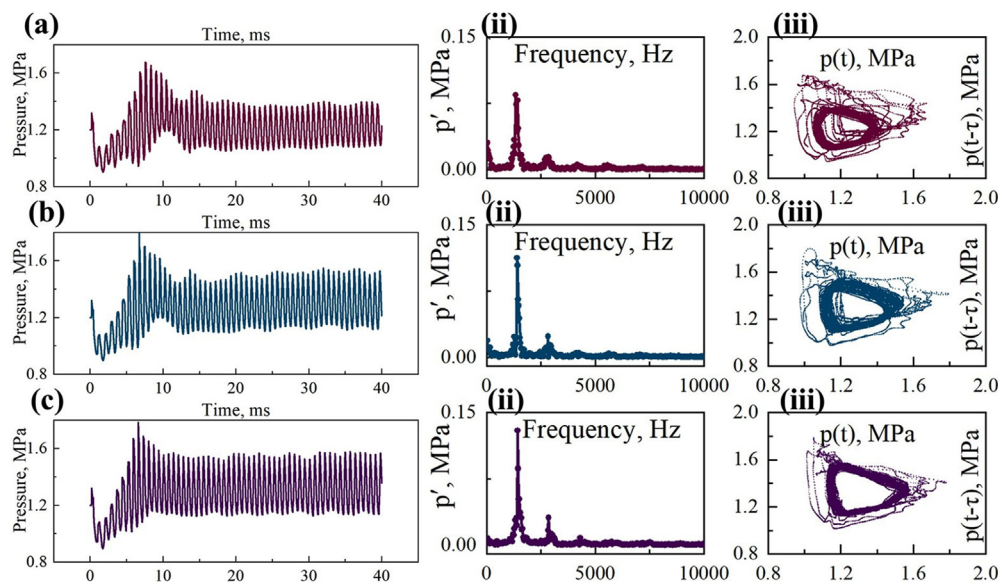
FIG 3. Time series of pressure monitored at probe 1 under different meshes in T = 900 K condition: (a) mesh 1, (b) mesh 2, and (c) mesh 3; (ii) amplitude spectrum using FFT algorithm; and (iii) phase diagram. Data were sampled over a time interval ranging from 5 to 40 ms. The time lag τ is equal to one-quarter of an oscillation period.
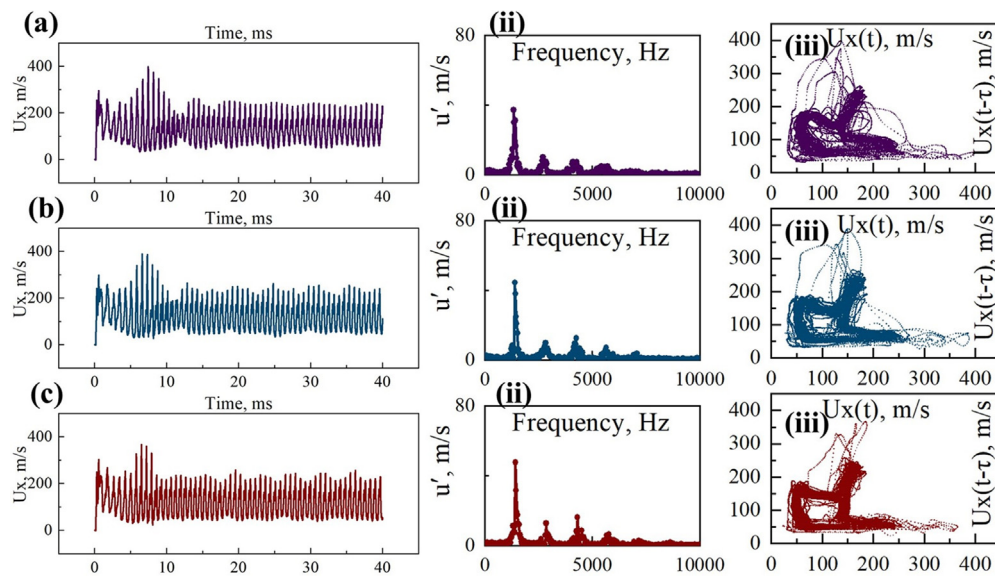
FIG. 4. Time series of axial velocity monitored at probe 2 under different meshes in T = 900 K condition: (a) mesh 1, (b) mesh 2, and (c) mesh 3; (ii) amplitude spectrum using FFT algorithm; and (iii) phase diagram. Data were sampled over a time interval ranging from 5 to 40 ms. The time lag τ is equal to one-quarter of an oscillation period.

broadband noise at lower frequencies due to alignment with longitudinal acoustic wave propagation direction. With increasing oxidizer inlet temperature, viscosity and density decrease, leading to higher Reynolds number for jet flow, which strengthens global instability mode of the system. Consequently, there is a significant increase in frequency peak value within the velocity spectrum along with frequency rising from 7371 Hz (T = 750 K) to 10,027 Hz (T = 1350 K). To provide scientific rigor, Figs. 5(d)–5(f) and 5(j)–5(l) illustrate the time series of velocity monitored at probe 3 along with the corresponding FFT results. The turbulent motion is stochastic; therefore, probe 3 was strategically positioned downstream of probe 2. As the vortex traverses from probes 2 to 3, it undergoes convection and merges with other vortices. Consequently, the amplitude of velocity oscillations at probe 3 surpasses that observed at probe 2. However, the spectral characteristics at both probe locations exhibit qualitative consistency, demonstrating that the y-directional velocity responds to vortex dynamics evolution as well as the monotonic variation in vortex shedding frequency with oxidizer inlet temperatures.

From the previous analysis, we observe that it is scientifically rigorous to use the y-direction velocity as a quantitative measure of vortex motion compared to the axial velocity signal. The frequency corresponding to the maximum peak of its frequency spectrum is identified as the vortex shedding frequency, which has also been widely adopted in the previous literature.[41,57,58,67] The frequency of vortex shedding, as measured by both probes, shows a monotonically increasing trend with an increase in oxidizer inlet temperature, as seen in Fig. 6. This is attributed to the higher jet temperature, which leads to a decrease in fluid viscosity and density, resulting in an increase in jet velocity and subsequently a higher frequency of vortex shedding. The measured vortex shedding frequency at probe 3 is slightly lower than that at probe 2 due to the enlarged geometric scale of the downstream merged vortices, leading to a reduced frequency. However, these findings do not alter the conclusions drawn in this paper regarding the impact of

probe location on vortex shedding frequency. Therefore, for accurate quantitative analysis of vortex dynamics, measurements were taken for y-directional velocity at probe 1.

C. Transition from combustion noise state to period-1 oscillation via intermittency

In a subsequent analysis, we investigated the impact of different oxidizer inlet temperatures on thermoacoustic instability under firing conditions. We observed that as the oxidizer inlet temperature increased from 700 to 900 K, there was a transition in system dynamics from the state of combustion noise (T = 700 K) to limit cycle states (T = 825, 850, and 900 K), which was preceded by intermittency (T = 750 and 800 K). Subsequently, we synchronized the examination of velocity oscillations and heat release oscillations at the shear layer to assess their dynamical states. The spatiotemporal dynamics of thermoacoustic systems during the transition routes to limit cycles revealed frequency-locking phenomena between pressure, velocity, and heat release.

Figure 7 shows an overview of the system dynamics under different oxidizer inlet temperatures (T). Upon inspecting the time traces of pressure, normalized fast Fourier transform (FFT) results, and phase diagram, we observe three different dynamical states as the oxidizer inlet temperature increases: a fixed point at T = 700 K, intermittency at T = 750 and 800 K, and a period-1 limit cycle at T = 825, 850, and 900 K. Next, we discuss the characterization of these dynamical states before examining vortex dynamics and heat release dynamics.

(1) Fixed point: Initially, at T = 700 K, the system is linearly stable and not in a state of spontaneous thermoacoustic instability. At this point, the gain of the positive feedback loop formed by the pressure and heat release is not strong enough to overcome the damping of the system.[4] During the onset of the combustion noise state in system dynamics, due to the stochastic nature of the turbulent motion, we observed: (i) non-periodic oscillations
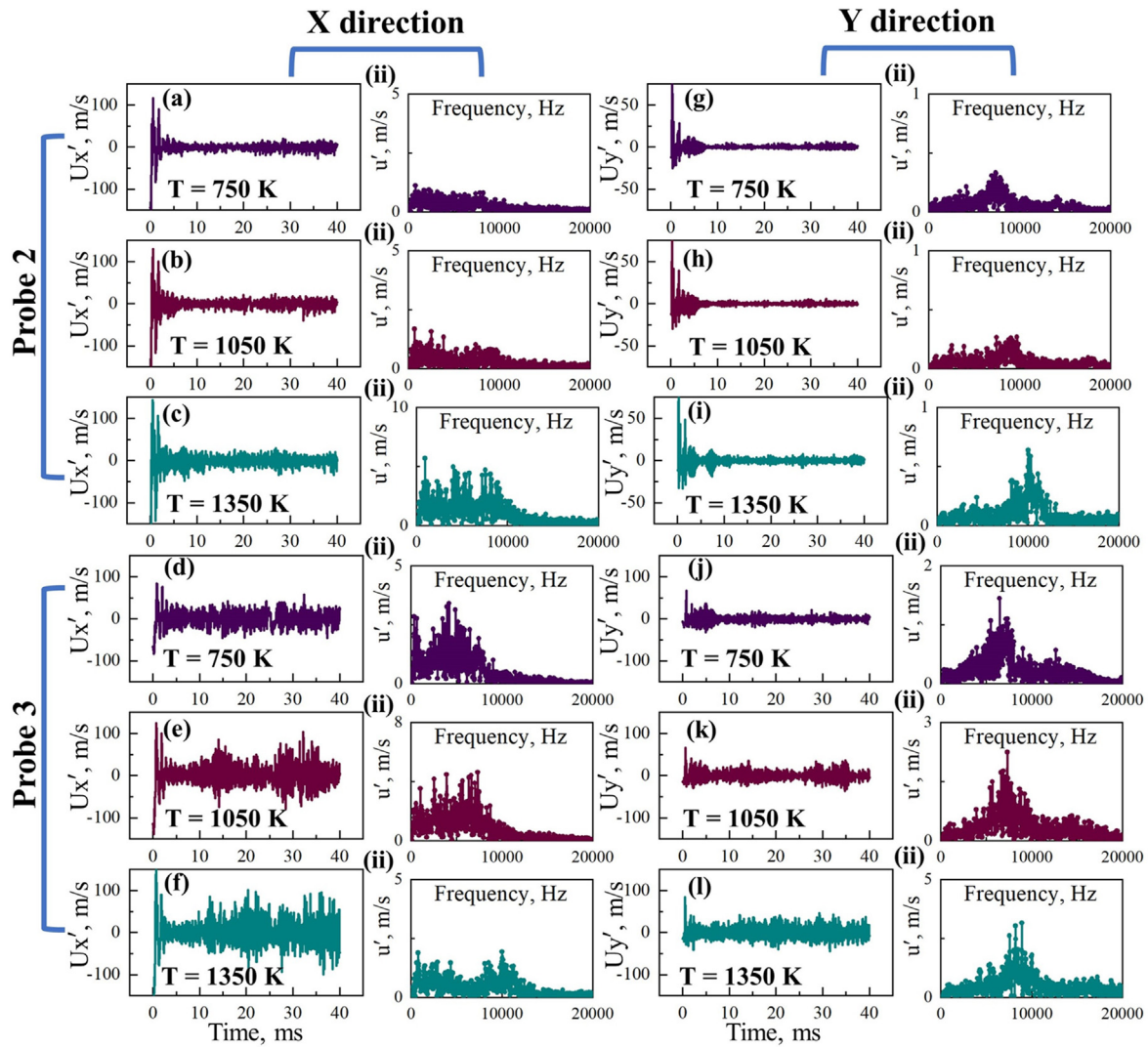
FIG. 5. (a)–(l) Time traces and (ii) corresponding FFT results monitored at probe 2 (a)–(c) and (g)–(i) and probe 3 (d)–(f) and (j)–(l) in the non-reacting flows: (a)–(f) the local axial velocity fluctuations as well as (g)–(l) the local y-th velocity fluctuations.
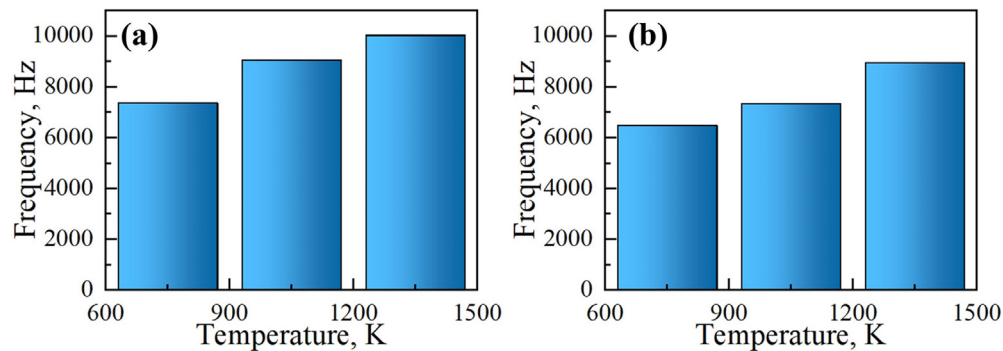
FIG. 6. Vortex shedding frequency under different oxidizer inlet temperatures in cold flow conditions: (a) probe 2 and (b) probe 3.
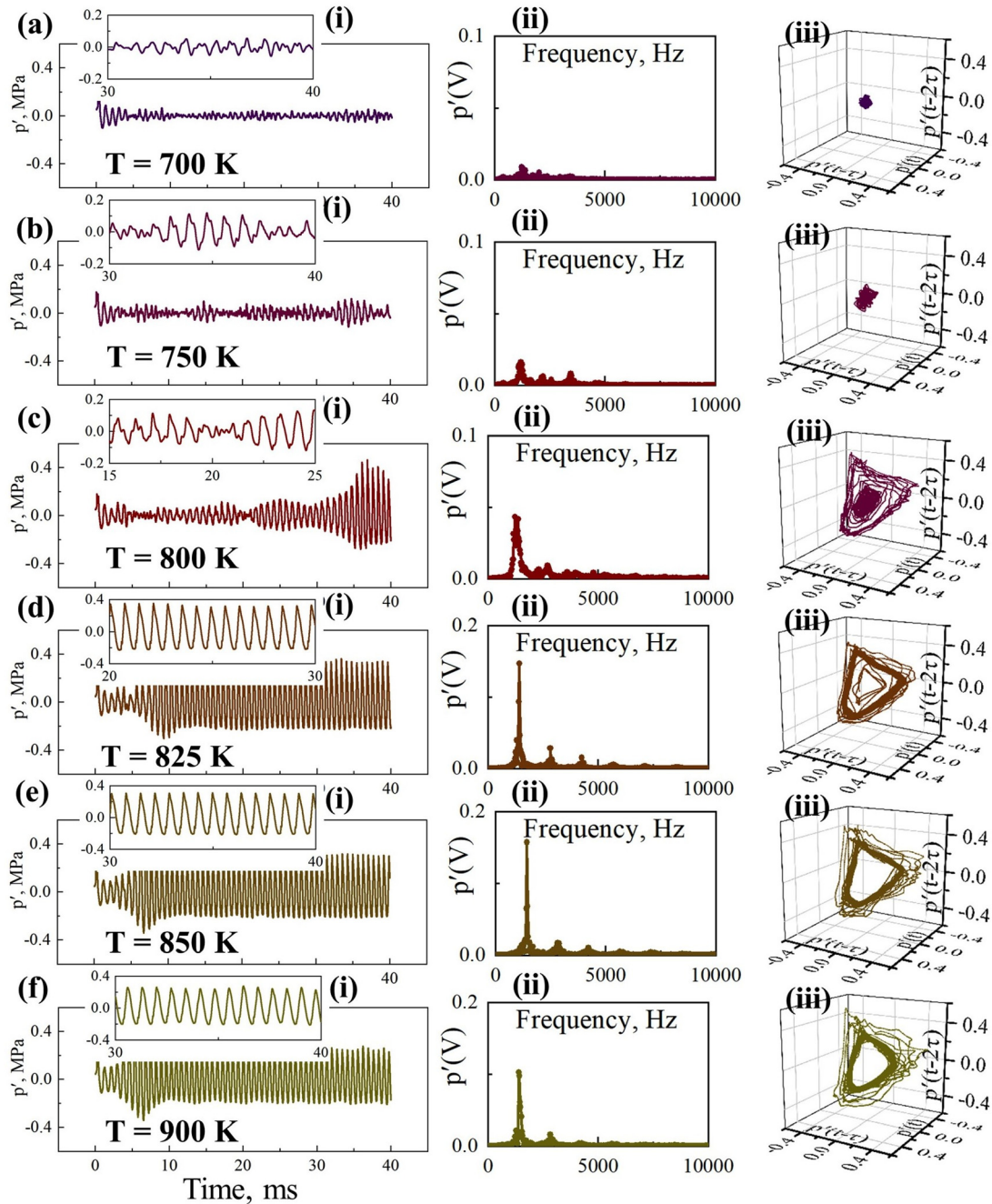
FIG. 7. Time series of pressure fluctuations monitored at probe 1 under different oxidizer inlet temperatures: (a) 700, (b) 750, (c) 800, (d) 825, (e) 850, and (f) 900 K; (i) enlarged time traces; (ii) normalized amplitude spectrum using FFT algorithm; and (iii) phase diagram. Data were sampled over a time interval ranging from 5 to 40 ms. The time lag τ is equal to one-quarter of an oscillation period.

with low amplitude, (ii) a broad-band noise rather than dominant peaks in the FFT results, and (iii) the presence of a ball-like structure in the embedding space of the phase diagram. These observations suggest that the system resides on a fixed-point attractor, which is disturbed by low levels of combustion noise.

(2) Intermittency: At higher oxidizer inlet temperatures ($750 \leq T \leq 800$ K), the thermoacoustic system becomes intermittent oscillation. The system dynamics alternates between two different states: fixed point and limit cycle states. This can be seen more clearly in the time traces (i), where bursts of medium amplitude period-1

oscillations appear intermittently over a background of low-amplitude fixed point. In phase diagram (iii), the system alternates between two different attractors: the fixed point at the core and the limit cycle around it. This is also demonstrated by the FFT results (ii), where a first-order acoustic mode dominates the FFT results with broadband peaks around it. In more detail, increasing the oxidizer inlet temperature amplifies and prolongs period-1 oscillations, even when both conditions are intermittent oscillations. As the different oxidizer inlet temperatures approach the thermoacoustic instability regime, the duration of these periodic oscillations continues for a longer period until the system fully transitions to a state of periodic oscillations.

(3) Period-1 limit cycle: At slightly higher oxidizer inlet temperatures ($825 \leq T \leq 900$ K), the thermoacoustic system becomes spontaneously unstable. The system dynamics transition from a state of combustion noise to thermoacoustic instability occurs through intermittency rather than Hopf bifurcation, which is traditionally believed to be the direct transition from the state of combustion noise to a limit cycle as control parameters vary. During the onset of thermoacoustic instability, we observed: (i) periodic pressure oscillations with high amplitude, (ii) the sharp peaks in the normalized FFT results, and (iii) the presence of a single-loop structure in the embedding space of the phase diagram. These observations indicate the limit cycle is period-1. In more detail, even in both period-1 limit cycle states, as we increase the oxidizer inlet temperatures, we observe three different normalized amplitudes of pressure oscillations: $0.1472 \rightarrow 0.1574 \rightarrow 0.1027$. The non-monotonic relationship between the amplitude of the limit cycle and oxidizer inlet temperature suggests a complex response in system dynamics. This phenomenon prompted us to conduct a synchronization examination among various subsystems of the combustion flow field, as well as to increase the oxidizer inlet temperature further to observe possible secondary bifurcations in system dynamics.

Figure 8 shows an overview of velocity traces and corresponding FFT results monitored at probe 2 under different oxidizer inlet temperatures ($700 \leq T \leq 900$ K). (1) Fixed point: At a temperature of 700 K, the velocities in the axial and y-directions continue to exhibit non-periodic oscillations with low amplitude due to intrinsic hydrodynamic instability. The spectral response of the axial velocity exhibits two distinct peaks at frequencies of 2371 and 1228 Hz, respectively. Based on the preceding analysis, it can be inferred that these frequencies closely correspond to the second-order and first-order acoustic frequencies of the combustion chamber. The coexistence of natural frequencies and its higher-order harmonics also implies complex nonlinear mechanism in turbulent thermoacoustic systems. The dominant frequency of the axial velocity is found at approximately the second-order acoustic frequency, while that of the y-th velocity is located near the third-order acoustic frequency. Interestingly, their non-coincidence can be attributed to turbulent motion's randomness. Conversely, the spectral responses of aperiodic oscillations exhibit broadband noise centered around the natural acoustic frequency, lacking distinct peaks or featuring multiple peaks. This phenomenon can be attributed to the low oxidizer inlet temperature, resulting in reduced flow velocity or Reynolds number at same mass flow rates and consequently diminishing the global hydrodynamic instability effect. (2) Intermittency: At $T = 750$ K, the dominant frequency of the axial velocity is 1114 Hz,

while that of the y-th velocity is 3428 Hz. The first-order acoustic frequency at this point is measured as 1200 Hz. Furthermore, it can be inferred that the dominant frequency of the axial velocity aligns closely with the first-order acoustic frequency, whereas that of the y-th velocity aligns closely with the third-order acoustic frequency. As we increase the oxidizer inlet temperature ($T = 800$ K), we observe a shift in dominant frequency for the y-th velocity to approximately 1371 Hz, which coincides with the first-order acoustic mode. Consequently, as we further increase the oxidizer inlet temperature, there is a gradual transition of vortex shedding's dominant frequency toward resonance with natural acoustic modes resulting in amplification and prolongation of period-1 oscillations. (3) Limit cycle state: Within the temperature range of 825–900 K, we observed the following phenomena: (i) periodic velocity oscillations characterized by significant amplitude and (ii) distinct peaks in both axial velocity and y-th velocity traces evident in the fast Fourier transform (FFT) analysis results. These observations suggest that the vortex shedding frequency associated with period-1 oscillations corresponds to the first-order acoustic frequency.

Figure 9 illustrates two different ways to characterize the y-th velocity signals, one as a phase diagram in nonlinear time series analysis (a)–(d) and the other as a short-time Fourier transform (i) in linear time series analysis to analyze the spectral composition and track their amplitude over time. (1) Fixed point: We observe in the short-time FFT results broadband characteristics with low amplitude concentrated near the 2 and 3L acoustic modes and no significant amplitudes are observed near the 1L acoustic modes. The phase space trajectories appear to be irregular, exhibiting multiple centers of rotation around their origin [$(u'(t), u'(t - \tau)) = (0, 0)$]. (2) Limit cycle state: During the onset of thermoacoustic instability, we observe a peak frequency near the 1L mode that oscillates significantly almost from the beginning, representing strong coupling. The phase diagram also shows a clear repeating pattern, resembling a bow-tie structure. Notably, this phenomenon has been previously documented and discussed in laboratory-scale liquid rocket engines by Kasthuri *et al.*[35] who observed a trefoil-knotlike-shape structure of phase space trajectory of pressure signal. This discrepancy arises due to high-amplitude acoustic oscillations compressing steepened pressure wavefront, leading to the formation of shock waves. Hence, based on the findings of this paper, it can be deduced that the velocity waveform exhibits significant non-linearity during thermoacoustic instability. This is characterized by the presence of steepened wavefronts in the velocity waveform, ultimately resulting in shock wave formation. (3) Intermittency: Based on the results of the short-time Fourier transform, we can observe intermittent bursts of periodic oscillations with medium amplitude occurring intermittently during two intermittent states ($T = 750$, $T = 800$ K), amidst non-periodic fluctuations that appear random. These bursts are reflected as intermittent peaks in the time-spectrum. During the non-periodic oscillations, low amplitudes are observed with broadbands in the spectrum. However, as bursts of periodic oscillations appear, the amplitude of oscillations near natural acoustic frequencies increases. Notably, at $T = 750$ K, the frequency of periodic oscillation bursts sequentially approaches 2 and 3L over time. At $T = 800$ K, initially, the frequency of periodic oscillation bursts is near 3L and then becomes concentrated near 1L. Combined with previous pressure trace analyses' results, it can be inferred that moderate to lower amplitude pressure oscillations during the onset of intermittent oscillations are driven by vortex shedding of higher-order harmonics (2 and 3L), while
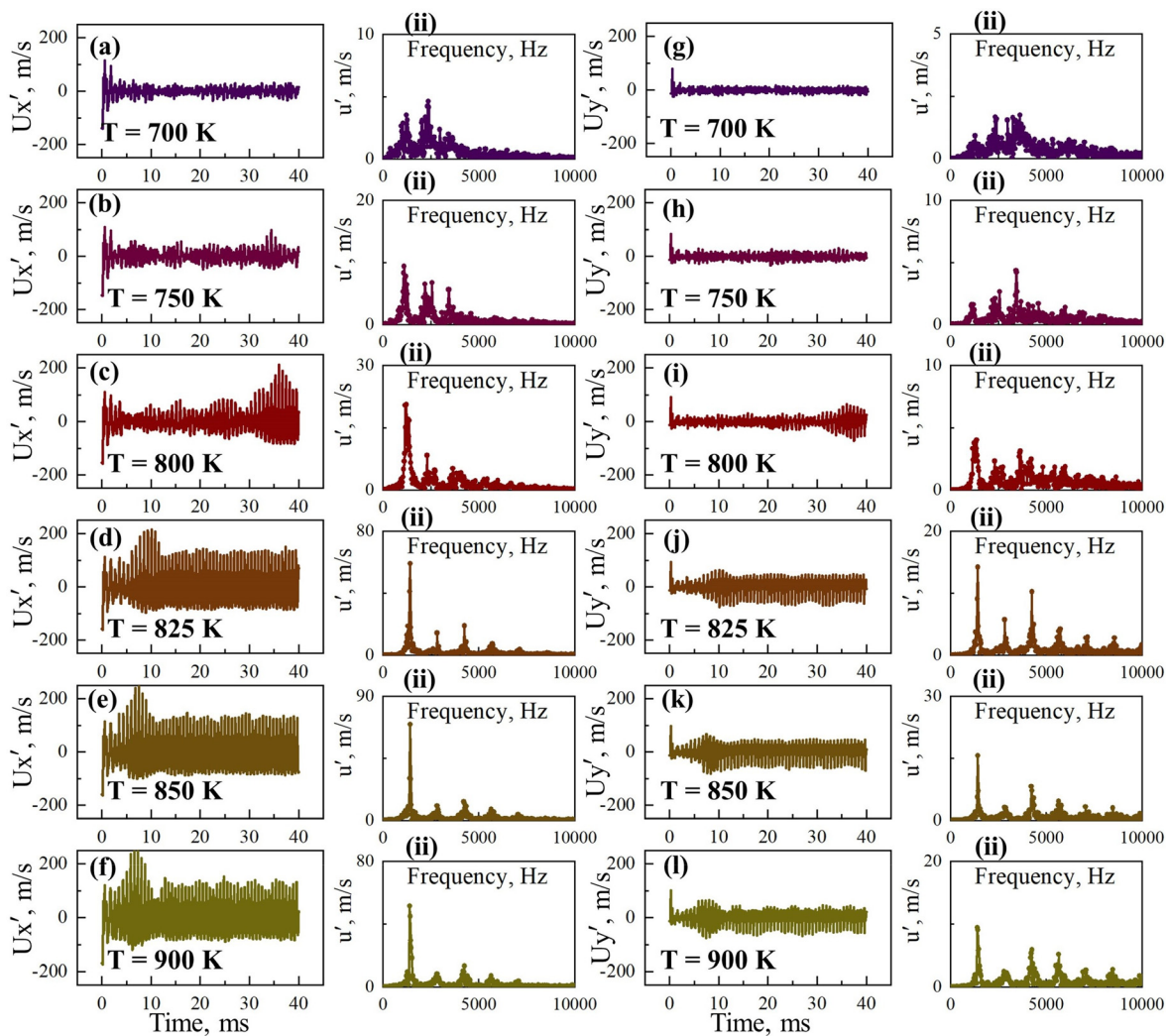
FIG. 8. Time series of axial velocity fluctuations and y-th velocity fluctuations monitored at probe 2 under different oxidizer inlet temperatures: (a) and (g) 700, (b) and (h) 750, (c) and (i) 800, (d) and (j) 825, (e) and (k) 850, and (f) and (l) 900 K; (ii) amplitude spectrum using FFT algorithm; data were sampled over a time interval ranging from 5 to 40 ms.

higher-amplitude pressure oscillations are driven by vortex shedding of first-order harmonics (1L). The phase diagram results for intermittent oscillations also indicate that as the duration of periodic oscillation bursts increases over time, there is a transition from a fixed point-like phase diagram to that resembling a limit cycle state.

Next, we examined the flame dynamics, where the local heat release rate monitored at probes 2 and 3 was present to provide a quantitative characterization of the flame response at different spatial locations. Figure 10 shows an overview of flame dynamics monitored at probe 2 (a)–(f) and probe 3 (g)–(l) under different oxidizer inlet temperatures ($700 \leq T \leq 900$ K), including the time traces of heat release rate (HRR), and normalized fast Fourier transform (FFT) results (ii). (1) Fixed point: At T = 700 K, the heat release rate (HRR) exhibits non-periodic oscillations with low amplitude monitored at probe 2 [Fig. 10(a)]. The FFT analysis reveals a first dominant peak at

2400 Hz accompanied by broadband noise. The local flame dynamics monitored at probe 3 become intermittent oscillations [Fig. 10(g)]. This is evidenced by the time traces, where bursts of medium amplitude aperiodic oscillations appear intermittently over a background noise with low amplitude The presence of chaotic oscillations is evident for both high-amplitude oscillations and low-amplitude noise, as indicated by the broadband noise observed in the FFT results (ii). This highlights the intricate spatiotemporal dynamics of the flame, even during combustion noise. (2) Intermittency prior to thermoacoustic instability: At $750 \leq T \leq 800$ K, the time series of heat release exhibits two distinct behaviors. During the period part of pressure oscillations, the heat release rate monitored by probe 2 oscillates in a periodic manner along with moderate amplitudes. During non-periodic oscillations of pressure traces, little heat release perturbation is observed. As the oxidizer inlet temperatures approach thermoacoustic instability

09 January 2025 08:14:45
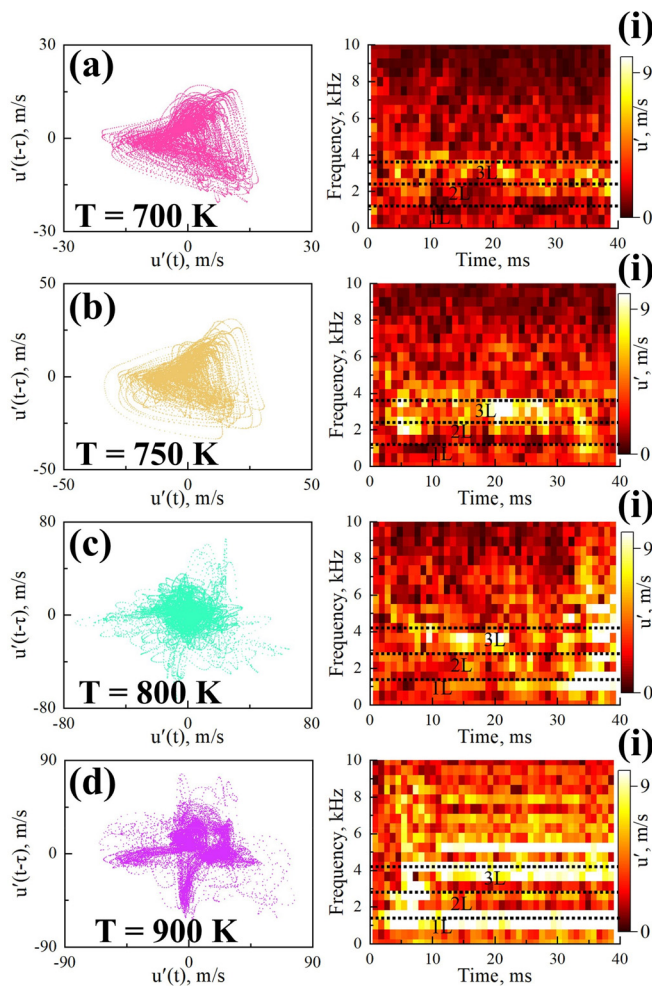
FIG. 9. Phase diagram of y-th velocity fluctuation data monitored at probe 2 and (ii) the short-time Fourier transform results corresponding to the states of (a) combustion noise state (T = 700 K), (b) and (c) intermittent oscillation states (T = 750, 800 K), (d) limit cycle state (T = 900 K). The time lag τ is equal to one-quarter of an oscillation period. The black broken lines represent the acoustic frequencies of the first three orders: 1, 2, and 3L.

regime, the duration of these periodic oscillations continues for a longer period until the system fully transitions to a state of periodic oscillations. At T = 750 K, the first two dominant frequencies in the FFT results are 3457 and 1257 Hz as shown in (b), (ii). At T = 800 K, the first dominant frequency is 1371 Hz, and the second dominant frequency is 3628 Hz as shown in (c), (ii). It can be further deduced that modulation of oscillation amplitude shifts the dominant frequency of heat release from higher-order harmonics to the first-order natural acoustic mode. As the heat release position develops downstream and is monitored by probe 3 (right side), the amplitude of the heat release perturbation increases significantly. At T = 750 K, although a medium amplitude HRR oscillation is observed, it was subsequently proved by FFT results that this was a non-period oscillation accompanied by a broadband spectrum as shown in (h), (ii). When the oxidizer inlet temperature approaches the thermoacoustic instability region (T = 800 K),

high-amplitude HRR oscillations accompanied by periodic acoustic oscillations and medium amplitude HRR oscillations accompanied by aperiodic pressure oscillations are observed as shown in (i), (ii). Broadband frequency spectrum is replaced by first-order acoustic frequency. (3) Limit cycle: At $825 \leq T \leq 900$ K, during the onset of thermoacoustic instability, we observed: (i) periodic HRR oscillations and (ii) the sharp peaks in the normalized FFT result. Notice that probe 2 is located near the initial shear layer. As the heat release position moves downward, the oscillation amplitude of probe 3 is higher than that of probe 2.

The combustion flow dynamics at frequency-locking can be examined via the relationship between acoustic fields, hydrodynamic instability, and combustion. This is shown in the lock-in map in Fig. 11. During the initial onset of combustion noise, the acoustic field, heat release, and hydrodynamic instability are not frequency-locked. The heat release oscillates at a second-order harmonic acoustic frequency, while the vortex shedding frequency is close to a third-order harmonic. During thermoacoustic instability, the acoustic field, heat release, and hydrodynamic instability are completely locked at the first-order acoustic frequency, while for T = 900 K condition, there is a slight reduction in the first-order dominant frequency. During intermittency, at a lower oxidizer inlet temperature (T = 750 K), the heat release and hydrodynamic oscillations are locked around the third-order harmonics with a slight offset. With a further increase in the oxidizer temperature (T = 800 K), the heat release and hydrodynamic oscillations lock around the first-order harmonics and are slightly higher. Elevating the oxidizer inlet temperature during intermittent oscillations results in a shift of frequency-locking from higher-order harmonics to near the first-order acoustic mode, thereby enhancing the thermoacoustic effect. It is noteworthy that both frequency-locking near higher-order harmonics and first-order acoustic frequencies are shifted from natural acoustic modes, leading to weak thermoacoustic instability, which is distinct from complete limit cycle states.

D. Second bifurcation from period-1 oscillation back to combustion noise state also via intermittency

In our previous discussion, we explored the intermittency routes from combustion noise to limit cycle states as the oxidizer inlet temperature increases and the phenomenon of frequency-locking between combustion flow subsystems. It raises a natural question whether a second bifurcation in the system leads to more complex nonlinear states as the oxidizer inlet temperature continues to increase. Figure 12 shows an overview of the second bifurcation of the system dynamics for different oxidizer inlet temperatures ($950 \leq T \leq 1450$ K). As the oxidizer inlet temperature continued to increase, we observed two different dynamical states: intermittent oscillations ($950 \leq T \leq 1150$ K) and fixed points ($1250 \leq T \leq 1450$ K). Our previous analysis revealed that as the oxidizer inlet temperature was increased, the occurrence of thermoacoustic instability was presaged by intermittency. Here, a second bifurcation occurs as we continue to increase the oxidizer inlet temperature, where the intermittency also presages the appearance of combustion noise. Within the intermittent oscillations post to the thermoacoustic instability regime, as the oxidizer inlet temperature approaches the fixed point, the duration of the low-amplitude, non-periodic oscillations gradually increases and eventually replaces the period-1 oscillations. The system dynamics of the liquid rocket engines
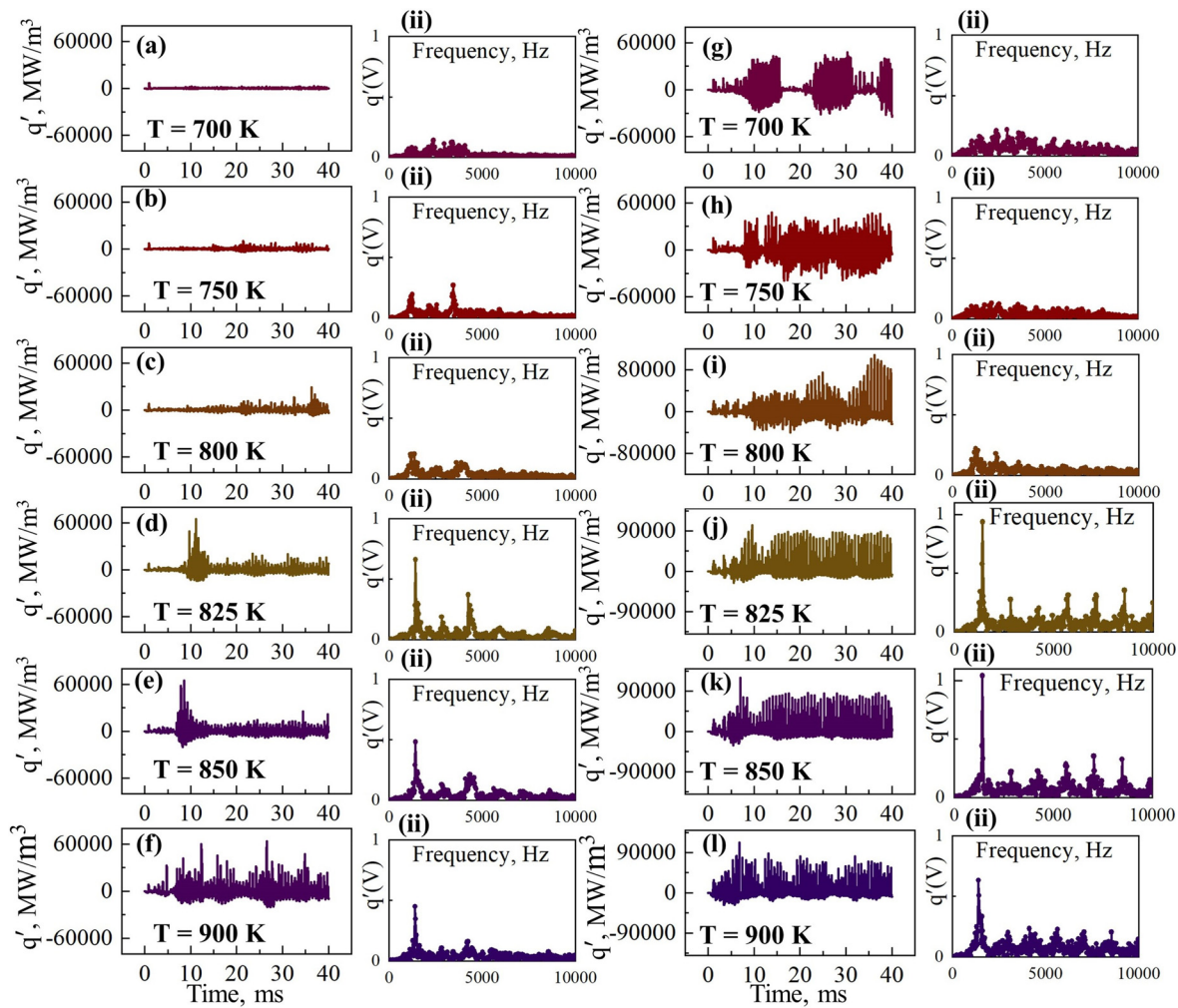
FIG. 10. Time series of heat release rate fluctuations (q') monitored at probe 2 (a)–(f) and probe 3 (g)–(l) under different oxidizer inlet temperatures: (a) and (g) 700, (b) and (h) 750, (c) and (i) 800, (d) and (j) 825, (e) and (k) 850, and (f) and (l) 900 K; (ii) normalized amplitude spectrum using FFT algorithm. Data were sampled over a time interval ranging from 5 to 40 ms. The time lag τ is equal to one quarter of an oscillation period.
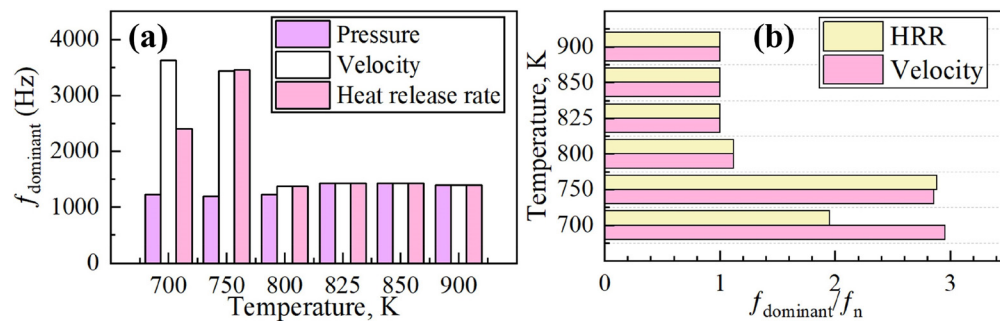
FIG. 11. Frequency-locking diagram between acoustic fields, local heat release rate, and vortex shedding monitored at probe 2 under different oxidizer inlet temperatures ($700 \leq T \leq 900$ K): (a) the first-order dominant frequency and (b) corresponding lock-in map. f_n represents the first-order dominant acoustic frequency.
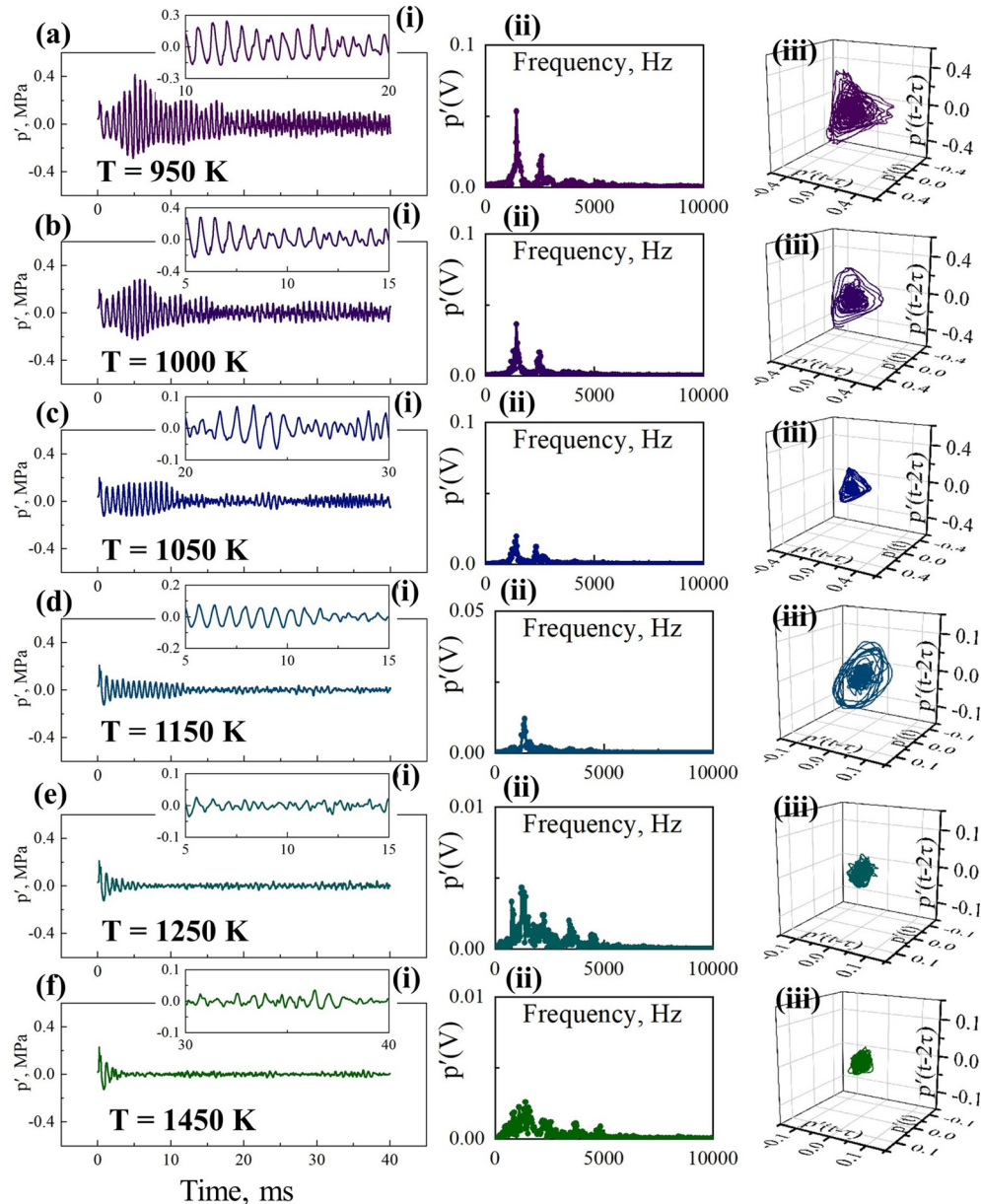
FIG. 12. Time series of pressure fluctuations monitored at probe 1 under different oxidizer inlet temperatures: (a) 950, (b) 1000, (c) 1050, (d) 1150, (e) 1250, and (f) 1450 K; (i) enlarged time traces; (ii) normalized amplitude spectrum using FFT algorithm; and (iii) phase diagram. Data were sampled over a time interval ranging from 5 to 40 ms. The time lag τ is equal to one quarter of an oscillation period.

exhibit intermittency routes both before and after the thermoacoustic instability under varying oxidizer inlet temperatures.

Figure 13 shows an overview of the time series of velocity fluctuations and FFT results under different oxidizer inlet temperatures ($950 \leq T \leq 1450\,\text{K}$). (1) Intermittency: at $950 \leq T \leq 1150\,\text{K}$, the amplitude of the velocity oscillations decreases as the oxidizer inlet temperature increases, which is attributed to a weak thermoacoustic effect. In more detail, when the system reaches intermittency, the

amplitude of the velocity oscillations during the onset of the period-1 oscillations is significantly larger than the amplitude of the oscillations during the occurrence of non-period oscillation. As the oxidizer inlet temperature increases, the duration of the non-periodic low-amplitude velocity oscillations is elongated, eventually almost completely replacing the high-amplitude velocity oscillations. This is also proved by the FFT results. At $T = 950\,\text{K}$, the FFT results for axial velocity oscillation exhibit two dominant frequencies: one at 1428 Hz and the other at
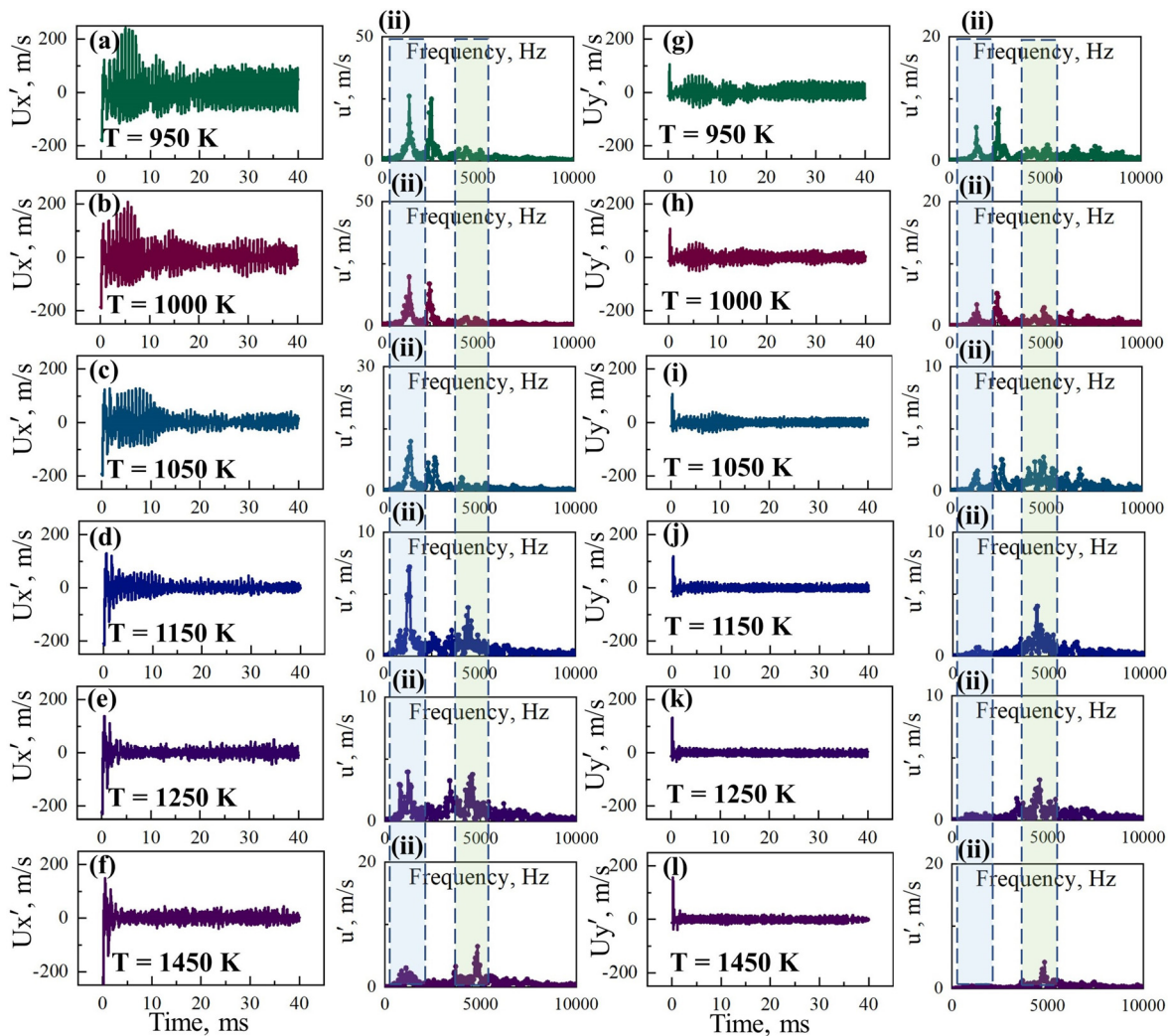
FIG. 13. Time series of axial velocity fluctuations and y-th velocity fluctuations monitored at probe 2 under different oxidizer inlet temperatures: (a) and (g) 950, (b) and (h) 1000, (c) and (i) 1050, (d) and (j) 1150, (e) and (k) 1250, and (f) and (l) 1450 K; (ii) amplitude spectrum using FFT algorithm; data were sampled over a time interval ranging from 5 to 40 ms.

2600 Hz. The first two orders of dominant frequency of radial velocity are 2600 and 1428 Hz. As the oxidizer inlet temperature increases, at T = 1150 K, the first two orders of dominant frequencies for axial velocities are 1371 and 4428 Hz, while the FFT results for radial velocities are completely dominated by 4428 Hz. It is worth noting that the peak values are barely observed near the natural first-order acoustic frequency (1L). (2) Fixed point: At $1250 \leq T \leq 1450$ K, we observe the smallest oscillation amplitude at the axial velocity and the y-th velocity. At T = 1250 K, the first two dominant frequencies for axial velocity are 1200 and 4600 Hz i.e., near the first-order acoustic frequency and near the third-order acoustic frequency, respectively, whereas the FFT results for radial velocity are completely dominated by 4600 Hz (3L). At T = 1450 K, the FFT results for both axial and radial velocities are completely dominated by 4857 Hz near the third-order harmonics.

Figure 14 illustrates the characteristics of the y-th velocity signal for different dynamical states after the thermoacoustic instability regime: (a) and (b) intermittency and (c) fixed point. (1) Intermittency: At T = 950 K, the short-time FFT results present the time evolution of the vortex dynamics during the intermittency, the vortex dynamics driven by the 1L mode gives way to the 2L mode, resulting in a reduction in the amplitude of the pressure oscillation. Similarly, at T = 1050 K, the vortex dynamics driven by the 2L mode at the beginning gives way over time to the 3L mode. The phase diagram of intermittent oscillations falls between the fixed point and the limit cycle state, resulting from transitions between the two. Meanwhile, whether the phase diagram structure is more similar to the fixed point, or the limit cycle state depends on the duration of periodic oscillations with high amplitude. (2) Fixed point: At the fixed point after the thermoacoustic instability (T = 1450 K), vortex shedding is
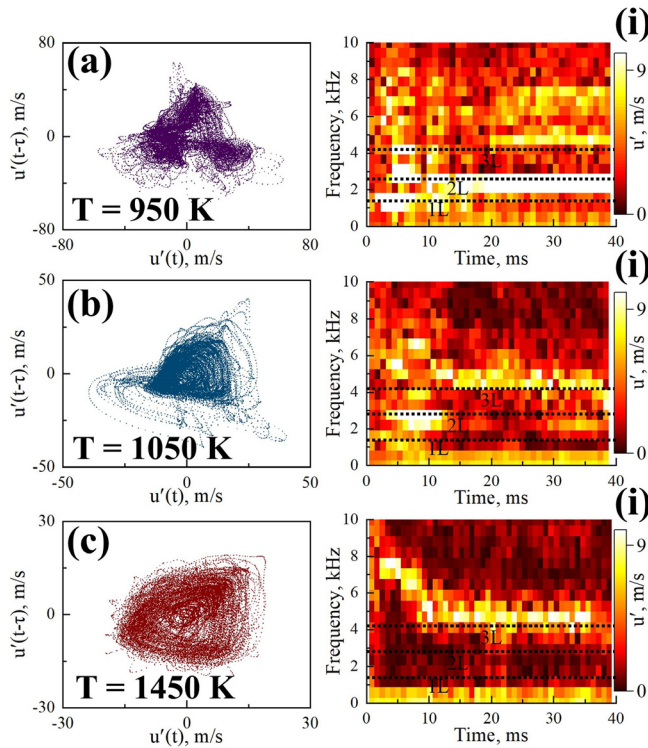
FIG. 14. Phase diagram of y-th velocity fluctuation data monitored at probe 2 and (ii) the short-time Fourier transform results corresponding to the states after the occurrence of limit cycle state: (a) and (b) intermittent oscillation states (T = 950, 1050 K) and (c) fixed point (T = 1450 K). The time lag τ is equal to one quarter of an oscillation period. The black broken lines represent the acoustic frequencies of the first three orders: 1, 2, and 3L.

initially driven by the intrinsically hydrodynamically unstable mode ($\sim$10 kHz), which gives way to the 3L mode neighborhood as time evolves.

Figure 15 shows an overview of HRR fluctuations monitored at probe 2 (left side) and probe 3 (right side) after thermoacoustic instability regime. (1) Intermittency: during the onset of intermittency post thermoacoustic instability regime ($950 \leq T \leq 1150$ K), we observe the loss of periodic repetitive patterns of heat release perturbations. As the oxidizer inlet temperature increases, the dominant frequency of the heat release gives way from 1400 Hz (1L) dominance (T = 950 K) to near 2L mode (T = 1000, 1050 K) and eventually near 4428 Hz (T = 1150 K). The second interesting point is that we also observe a gradual increase in the amplitude of the oscillations of HRR without considering the amplitude of the acoustic perturbation, which represents a change in the anchoring point of the flame, as will be expanded in detail in the snapshot analysis later. (2) Fixed point ($1250 \leq T \leq 1450$ K): At the fixed point post the thermoacoustic instability region, notable distinctions arise in terms of high-amplitude perturbations observed in the heat release rate (HRR), while the dominant frequency is completely dominated by $f \approx 5000$ Hz. Probe 3 is downstream of probe 2 and therefore more complex in terms of spectral response.

Frequency-locking diagrams after the thermoacoustic instability regime are shown in Fig. 16. In the intermittent region following

thermoacoustic instability, initially at a temperature of 950 K, the frequency of vortex shedding is close to that of the second longitudinal (2L) acoustic mode, while the dominant frequency of heat release rate (HRR) remains near the first longitudinal (1L) mode. At slightly higher oxidizer inlet temperatures (T = 1000 K), both HRR and vortex shedding frequencies are fully locked in near the second-order acoustic frequency. When T = 1050 K, the dominant frequency of vortex dynamics is located between the third-order longitudinal (3L) and fourth-order longitudinal (4L) modes, while HRR still remains slightly lower than that of 2L mode. A slight increase in oxidant inlet temperature to 1150 K causes heat release dynamics to be fully locked in 2L mode, while vortex dynamics remain between 3 and 4L modes. As temperature increases further, system dynamics reach fixed point states where both heat release and vortex dynamics are fully locked in a higher-order mode between 3 and 4L modes rather than being fully natural acoustic.

E. Evidence from combustion flow fields

In this section, we present evidence from combustion flow fields to identify relevant instability mechanisms. On the one hand, we calculated the mixture fraction and flame index to gain deeper insight into flame dynamics. We also introduced periodic snapshot analysis to explore the time evolution of the combustion flow fields. On the other hand, we examined transport equations for vorticity, where baroclinic torque is considered as the main reason for maintaining instability.

1. Flame dynamics

To facilitate the discussion later, we present the mathematical expression of the local mixture fraction as follows:[27,28]

$$Z = \frac{v_{st} Y_{C_{12}H_{26}} - Y_{O_2} + Y_{O_2}^0}{v_{st} Y_{C_{12}H_{26}}^0 + Y_{O_2}^0}, \quad (7)$$

where $v_{st} = 3.5$, $Y_{C_{12}H_{26}}^0 = 1.0$, and $Y_{O_2}^0 = 0.42$. $Y_{C_{12}H_{26}}$ and Y_{O_2} are the local mass fraction of n-dodecane and oxygen, respectively. The stoichiometric mixture fraction is 0.107. On the fuel flow side, $Z = 1$, while on the oxidizer flow side, $Z = 0$. The examination of the mixture fraction allows the study of the mixing dynamics of the fuel as well as the oxidizer. We introduce the flame index to distinguish between diffusion flame and premixed flame. In this paper, following Nguyen and Sirignano[28] the flame index was combined with the heat release rate to avoid pseudo-flame structures. The mathematical expression is as follows:

$$NFI = \frac{\nabla Y_{C_{12}H_{26}} \cdot \nabla Y_{O_2}}{\left| \nabla Y_{C_{12}H_{26}} \cdot \nabla Y_{O_2} \right|} \cdot HRR, \quad (8)$$

where HRR denotes the heat release rate (W/m^3). $Y_{C_{12}H_{26}}$ denotes the local mass fraction of n-dodecane, and Y_{O_2} denotes the mass fraction of the oxygen. Positive values of NFI represent premixed flames, negative values represent diffusion flames, and 0 represents the absence of combustion. Flame index analysis provides an insight for analyzing burning modes in liquid-fueled combustors. Figure 17 shows the time series of pressure under three different working conditions. Five moments of interest are marked in the plots. The three operating conditions, respectively, correspond to the combustion noise state before
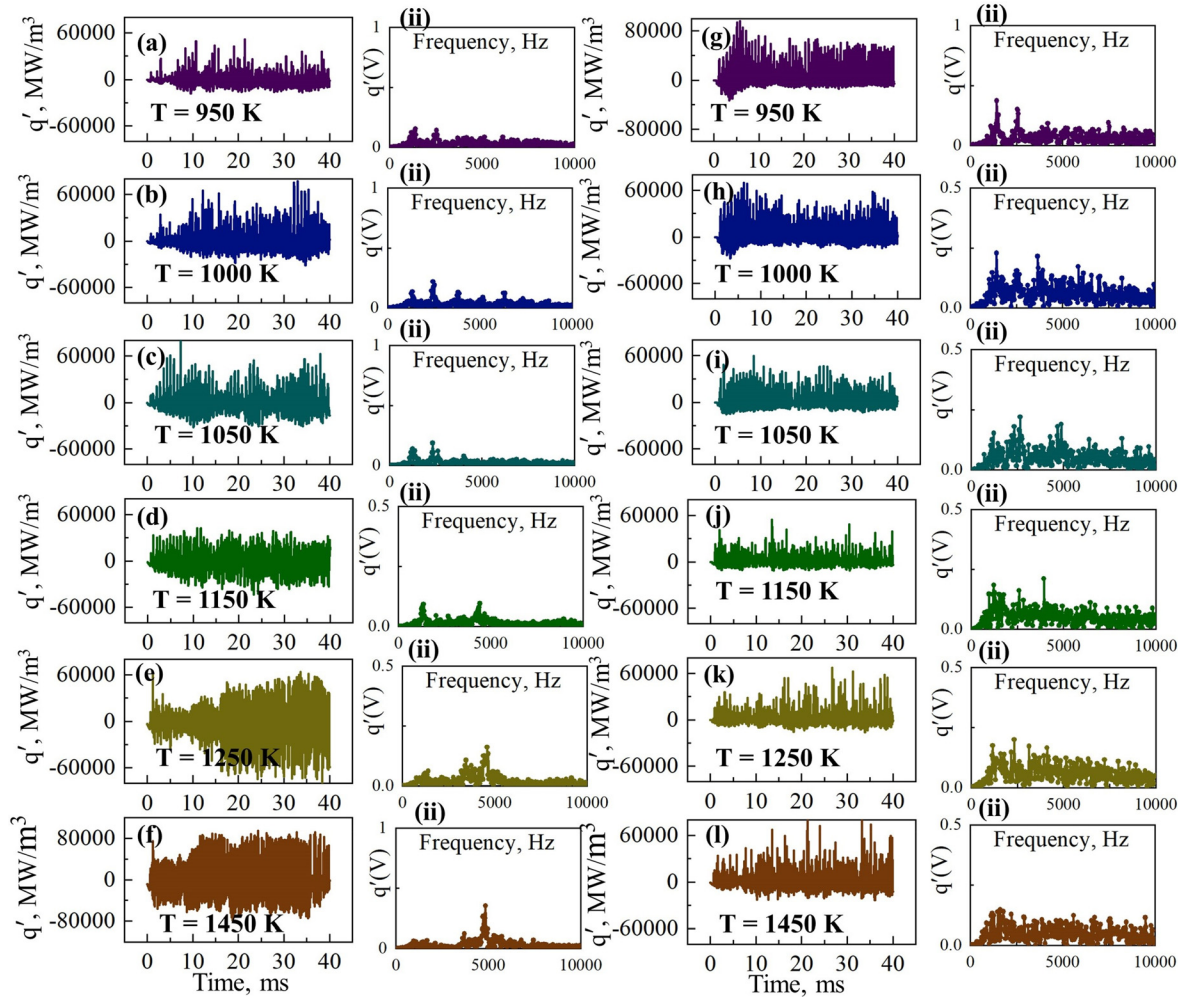
FIG. 15. Time series of heat release rate fluctuations (q') monitored at probe 2 (a)–(f) and probe 3 (g)–(l) under different oxidizer inlet temperatures: (a) and (g) 950, (b) and (h) 1000, (c) and (i) 1050, (d) and (j) 1150, (e) and (k) 1250, and (f) and (l) 1450 K; (ii) normalized amplitude spectrum using FFT algorithm. Data were sampled over a time interval ranging from 5 to 40 ms. The time lag τ is equal to one quarter of an oscillation period.
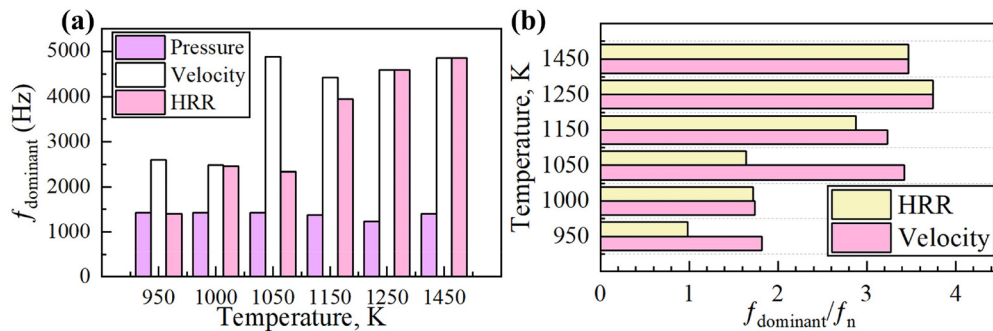
FIG. 16. Frequency-locking diagram between acoustic fields, local HRR, and vortex shedding monitored at probe 2 post thermoacoustic instability ($950 \leq T \leq 1450$ K): (a) the first-order dominant frequency and (b) corresponding lock-in map. f_n represents the first-order dominant acoustic frequency.
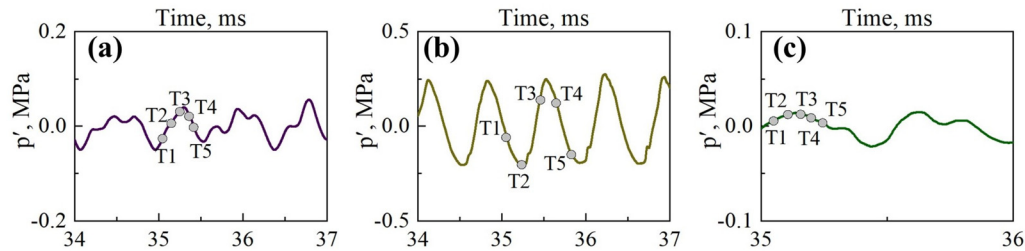
FIG. 17. Pressure traces monitored at probe 2 for different oxidizer inlet temperatures: (a) T = 700, (b) T = 900, (c) T = 1450 K. Each of the five moments of interest is marked.

the thermoacoustic regime, the thermoacoustic regime, and the combustion noise state after the thermoacoustic regime.

The flame dynamics during the regime of fixed point before the onset of limit cycle state are shown in Fig. 18. Coordinate variations along the axial direction range from −1 to 15 cm. We observe that the flame is fully anchored at the shear layer downstream of the dump plane due to the interaction of the high-velocity streams and the low-velocity streams. We also note that although the fuel and oxidizer have reached the mixture fraction at the equivalence ratio near the dump plane (x = 0 cm), combustion is rarely observed here. Snapshots of the NFI further reveal that premixed combustion is occurring. As the flow moves downstream, diffusion flames begin to appear. Five snapshots demonstrate the temporal evolution of the combustion flow field over a time interval of 0.35 ms. We observe perturbations in the flame front and small-scale vortex structures during the process of roll-up and downward convection.

The flame dynamics during the onset of thermoacoustic instability are shown in Fig. 19, where the oxidizer inlet temperature is 900 K. We observe that large-scale coherent structures are formed downstream of the dump plane in both mixture fraction snapshots and heat release snapshots. In earlier pioneering work,[14,56] it was also shown that large-scale coherent structures drive combustion instability in

such a dump combustor. The significantly increased heat release near the dump plane also strengthens thermoacoustic instability, as it is located at the antinode of the first-order acoustic modes. The time series of pressure in Fig. 17 indicate that the high-pressure wave is localized near the dump plane at T3 and T4, while the pressure wave propagates downstream of the combustion chamber and away from the dump plane at T1, T2, and T5. It is observed that when the pressure wave propagates near the dump plane, significant large-scale coherent structures are evident in both the mixture fraction and heat release distribution. In contrast, as the pressure wave moves away from the vicinity of the dump plane, the flame surface gradually becomes continuous and loses its wrinkles. This observation further highlights that acoustic oscillations within the combustion chamber play a crucial role in modulating the combustion field. More specifically, analysis of flame index cloud maps reveals coexistence of diffusion flames and premixed flames when high-pressure waves are present near the dump plane.

Figure 20 illustrates the flame dynamics in a combustion noise state after the occurrence of thermoacoustic instability, where the oxidizer inlet temperature is 1450 K. We observe continuously distributed flame fronts as well as small-scale vortex structures. The flame is fully anchored in the shear layer, from near the dump plane to downstream
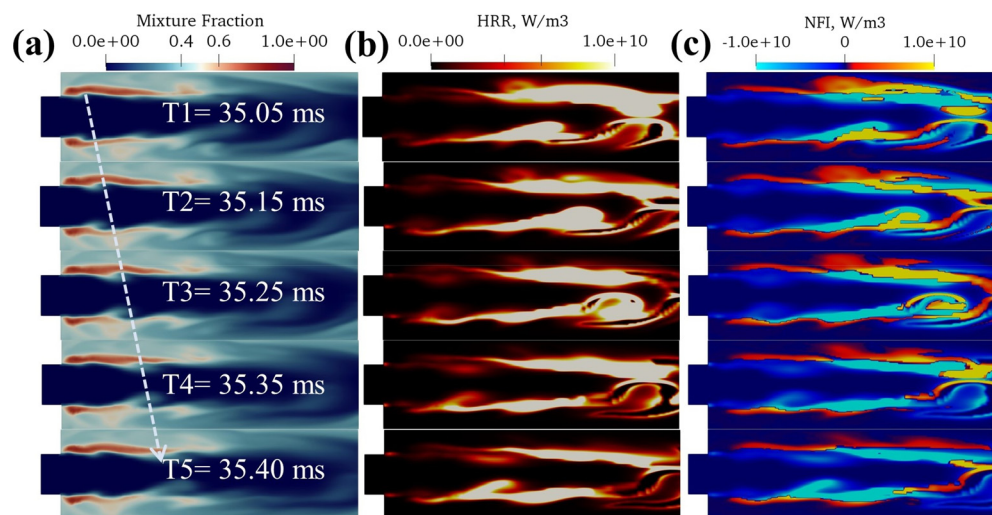
FIG. 18. Cycle snapshots during combustion noise state prior to thermoacoustic instability (T = 700 K). (a) Left images: Mixture fraction. (b) Middle images: heat release rate (W/m³). (c) Right images: NFI (W/m³).
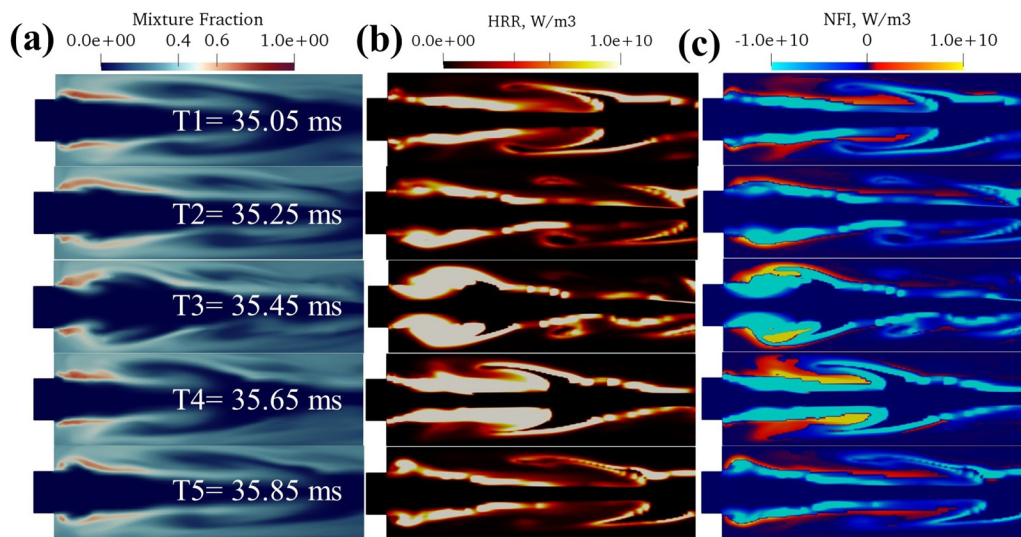
FIG. 19. Cycle snapshots during thermoacoustic instability (T = 900 K). (a) Left images: mixture fraction. (b) Middle images: heat release rate (W/m^3). (c) Right images: NFI (W/m^3).
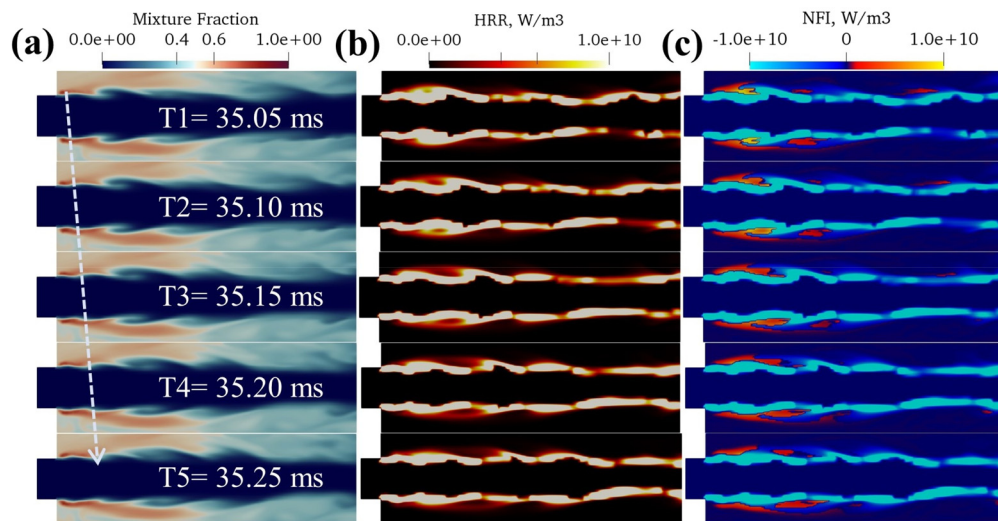
FIG. 20. Cycle snapshots during combustion noise state post to thermoacoustic instability (T = 1450 K). (a) Left images: mixture fraction. (b) Middle images: heat release rate (W/m^3). (c) Right images: NFI (W/m^3).

of the combustion chamber. The loss of large-scale coherent structure results in the lack of thermoacoustic instability. On the other hand, the increase in the oxidizer inlet temperature leads to a rapid evaporation of the liquid kerosene in the vicinity of the dump plane, as evidenced by the snapshots of the mixture fraction. In the snapshots of the flame index, we also hardly observe the presence of premixed flames. The perturbation of the flame front accompanied by the shedding of a complete vortex during one cycle at a time interval of 0.2 ms is also observed. Compared to the combustion noise condition before the thermoacoustic instability, the anchoring position of the flame is shifted toward the upstream of the combustion chamber, which is due

to the shortened heating time of the fuel caused by an increase in the temperature of the oxidizer.

Figure 21 further calculates the percentage fraction of premixed flame and diffusion flame for each of the above three conditions at time averaging. The time interval for sampling was 35–40 ms, and the sampling frequency was 20 kHz. The percentage fractions of the diffusion flame for the three operating conditions of T = 700, T = 900, and T = 1450 K were 85%, 97%, and 98.6%, respectively. Therefore, the increase in oxidizer inlet temperature promotes the formation of diffusion flame. The above results also indicate that diffusion flame is the dominant combustion mode for such a liquid-fueled combustor.
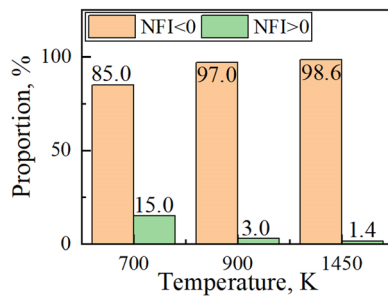
FIG. 21. Burning modes over the whole combustion chamber for different oxidizer inlet temperatures.

2. Vorticity transport

The generation of thermoacoustic instabilities depends on the emergence of large-scale coherent structures in liquid-fueled coaxial liquid rocket combustors. Large-scale coherent structures increase the fuel-oxidizer mixing and subsequent combustion heat release; hence, it is necessary to examine the vorticity transport equations in this section. The mathematical description of the vorticity transport equation in a compressible reacting flow without body forces is as follows:

$$\frac{d\boldsymbol{\omega}}{dt} = (\boldsymbol{\omega} \cdot \nabla)\boldsymbol{u} - \boldsymbol{\omega}(\nabla \cdot \boldsymbol{u}) + \frac{\nabla\rho \times \nabla p}{\rho^2} + \nabla \times \left(\frac{\nabla \cdot \boldsymbol{\tau}}{\rho}\right), \quad (9)$$

where d/dt denotes the material derivative operator, $\boldsymbol{u}$ is the flow velocity, ρ is the local fluid density, p is the local pressure, and $\boldsymbol{\tau}$ is the viscous stress tensor. The first term on the right-hand side represents vortex stretching of vorticity due to flow velocity gradients. The second term on the right-hand side describes the dilatation of vorticity caused by flow compressibility. The third term on the right-hand side is the baroclinic torque term, which accounts for changes in vorticity resulting from the intersection of density and pressure surfaces. The fourth term on the right-hand side accounts for vorticity diffusion due to viscous effects. Here, the first three terms on the right-hand side are all of interest in combustion flow fields with different pressure gradients, namely the vortex stretching term, the vortex dilatation term, and the baroclinic torque term.

Figure 22(a) shows the instantaneous spanwise vorticity contours for three different dynamical states under the high-pressure wave

located near dump plane. The slices shown in the figure are x-y planes with axial coordinates ranging from −1 to 15 cm. The main common features of these three states are the opposite sign at the upper and lower corners of the dump plane, as well as the reduction of spanwise vorticity further downstream. However, it can be observed that the spatial development of the vortex structure is jointly influenced by both the oxidizer inlet temperature and flame stability. In contrast to other cases, in the thermoacoustic instability case (T = 900 K), large-scale coherent structures emerge due to high-pressure waves near the shear layer, which suppresses small-scale vortex activity. In the combustion noise case (T = 1450 K) following thermoacoustic instability, it was observed that even small-scale vortex structures were completely anchored along the shear layer. For combustion noise case prior to thermoacoustic instability (T = 700 K), reduced flame-induced vorticity generation near the dump plane was observed due to decreased heat release from cold oxidizer inlet temperature. Figures 22(b)–22(d) show instantaneous contours of vortex stretching, dilatation, and baroclinic torque terms. The vortex stretching term is responsible for the distribution of vorticity and the transfer of energy between large-scale and small-scale vortices.[68] In all three conditions, it is produced downstream of the combustion chamber and is barely observable near the dump plane. In addition, it expands as the oxidizer inlet temperature increases, while the pressure gradient and combustion effects have little effect on this term. The dilatation term is a source of vorticity due to combustion, which arises from the density gradient across the flame front.[44] For a cold oxidizer inlet temperature (T = 700 K), the dilatation term arises in the initial shear layer and changes its sign downstream of the dump plane. Both the oxidizer inlet temperature and the pressure gradient have a significant effect on the dilatation term. For T = 900 K, the high-pressure wave advances the sign change downstream of the combustion chamber. For the combustion noise condition after the thermoacoustic instability (T = 1450 K), there is no significant sign change downstream of the combustion chamber. The baroclinic torque is another mechanism of vorticity induced by the flame, resulting from abrupt density and pressure gradients along the flame front.[69] The distribution of the baroclinic torque for the three conditions is mainly along the flame front with different signs, which is due to the density gradient between the unburned reactants and hot products. However, during thermoacoustic instability, the pressure gradient changes alter the spatial development of the baroclinic torque downstream of the dump plane: there is a thicker baroclinic torque
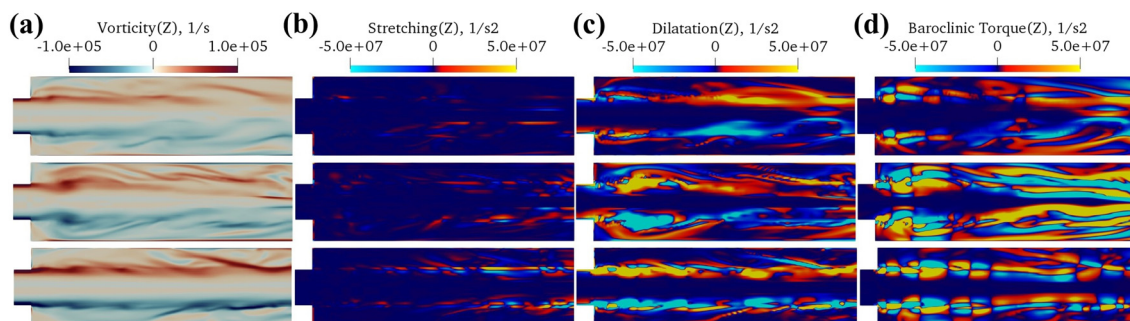
FIG. 22. (a) Instantaneous spanwise vorticity, (b) vortex stretching, (c) vortex dilatation, and (d) baroclinic torque under the high-pressure wave located near dump plane. Top to bottom: combustion noise state before thermoacoustic instability (T = 700 K), thermoacoustic instability (T = 900 K), and combustion noise state after thermoacoustic instability (T = 1450 K).

pattern along the flame front, which consequently leads to enhanced mixing and subsequent combustion that amplifies the instability. The study conducted by Harvazinski et al.[27] solely focused on comparing the impact of the baroclinic torque term on the combustion instability mechanism under the parameter space of the acoustic characteristics of the combustion chamber in a methane/oxygen single-element liquid rocket engine. In this paper, we further investigate various source terms in the vorticity transport equation and observe that, apart from the baroclinic torque term, the vortex dilatation term also plays a significant role in altering the inlet temperature of oxidizer in a gas-oxygen/liquid kerosene single-element liquid rocket engine.

IV. CONCLUSIONS

In this work, three-dimensional compressible large eddy simulation algorithms combined with the Euler–Lagrange framework are developed to study spontaneous thermoacoustic instability in a single-element liquid-fueled rocket combustor burning liquid kerosene and decomposed hydrogen peroxide. After validating the numerical framework and achieving grid independence, we focus on the effect of oxidizer inlet temperature on the (i) dynamic transition route before and after thermoacoustic regime, (ii) corresponding frequency-locking routes between acoustic perturbations, vortex dynamics and combustion heat release, and (iii) underlying physical mechanisms related to the transition of the system dynamics.

During the first bifurcation ($700 \leq T \leq 900$ K), we first observed the transition of the system dynamics from the combustion noise state (the fixed point, FP) to the limit cycle state (P1) via intermittency. In the FP before the thermoacoustic instability, vortex dynamics and heat release dynamics are driven by third-order (3L) and second-order (2L) acoustic modes, respectively, whereas at the onset of the P1 state, the heat release, vortex shedding, and acoustic oscillations are fully locked to the first-order (1L) acoustic mode. In particular, during the intermittency before the thermoacoustic instability, the heat release dynamics and vortex dynamics were locked near the natural acoustic mode but with a slight deviation. Furthermore, the short-time Fourier transform results for the velocity signal show a burst of periodic oscillations of intermittency associated with vortex dynamics driven by the 1L mode whereas vortex shedding driven by higher-order harmonics leads to the non-period oscillation of intermittency.

During the second bifurcation ($950 \leq T \leq 1450$ K), a transition of the system dynamics from the P1 state back to the FP state via intermittency was observed. To our knowledge, this is also the first report of the second bifurcation phenomenon in a liquid-fueled rocket combustor with subcritical turbulent spray combustion. After entering into intermittency following thermoacoustic instability, vortex dynamics were initially driven by the 2L mode but with some frequency bias. As the oxidizer inlet temperature increased, the frequency of vortex dynamics shifted between the 3L mode and 4L mode. The dominant frequency of heat release also transitioned to higher-order harmonics from the 1L mode. In FP state after thermoacoustic instability, both vortex dynamics and heat release dynamics had dominant frequencies locked between 3L mode and 4L mode. Short-time Fourier transform results for velocity signal showed that during intermittent periodic bursts, vortex dynamics were driven by lower-order acoustic modes, while during intermittent non-periodic background noise, they were also driven by broadband noise near higher-order harmonics.

Finally, we present a comprehensive analysis of the combustion flow fields. The results indicate that diffusion flames are the dominant combustion mode in liquid-fueled rocket combustors. This finding appears to deviate significantly from previous results for gas-phase fuels such as methane, where premixed flames were found to be dominant in standard experimental conditions at CVRC.[29] An increase in oxidizer inlet temperature further promotes the formation of diffusion flames. Large-scale coherent structures formed under P1 conditions were also observed in the flame dynamics snapshot analyses compared to FP states. Analyses of various source terms in the vorticity transport equation reveal that flame-induced vorticity generation, including vortex dilatation and baroclinic torque terms, dominates the combustion flow field. Other details of the combustion flow include (i) the flame anchoring point is moved forward toward the dumping plane due to the increase in oxidizer inlet temperature, (ii) the flame fronts in the FP state after the thermoacoustic instability region show a more continuous structure lacking wrinkles compared to the FP state prior to the thermoacoustic instability region, and (iii) the diffusion flames appear downstream of the combustion chamber while partially premixed flames occur near the shear layer. In conclusion, this paper provides a comprehensive study of the generation and dissipation of thermoacoustic instability due to oxidizer inlet temperature variations.

AUTHOR DECLARATIONS
Conflict of Interest

The authors have no conflicts to disclose.

Author Contributions

Yuanzhe Liu: Conceptualization (lead); Formal analysis (lead); Investigation (lead); Methodology (lead); Software (lead); Validation (lead); Writing – original draft (lead). **Pei-jin Liu:** Conceptualization (equal); Investigation (equal); Supervision (equal); Writing – review & editing (equal). **Zhuopu Wang:** Conceptualization (equal); Funding acquisition (equal); Methodology (equal); Supervision (equal); Writing – review & editing (equal). **Wen Ao:** Writing – review & editing (equal). **Yu Guan:** Supervision (equal); Writing – review & editing (equal).

DATA AVAILABILITY

The data that support the findings of this research are available from the corresponding author upon reasonable request.

APPENDIX: BENCHMARKS

This section provides a thorough examination of (i) the interaction of gas and liquid kerosene based on the Eulerian–Lagrangian framework, (ii) the global single-step kerosene/oxygen chemical reaction kinetics, and (iii) the ability to capture the spontaneous thermoacoustic instability.

1. Benchmark: Non-reacting spray A

In the section, we first simulated the standard ECN spray A condition under non-reactive conditions. In the spray A case, liquid kerosene ($C_{12}H_{26}$) was injected into the combustion chamber through a circular hole with a diameter of 90 μm at an injection pressure of 150 MPa, while the pressure in the combustion chamber was maintained at 6 MPa. A total of 3.5 mg of kerosene was injected into the combustion chamber with a time interval of 1.5 ms. The initial ambient conditions are shown in Table V. For a more detailed description of experiments, refer to the previous paper.[50,61]

09 January 2025 08:14:45

TABLE V. Initial condition of non-reactive spray A.

	Mass fraction of species (%)				Ambient temperature (K)	Ambient pressure (MPa)
Benchmark1	O_2	N_2	H_2O	CO_2		
	0	89.71	3.77	6.52	900	6.0

The computational domain was a cube with each side measuring 108 mm, which is the same size as the combustor in the experiment. The wall temperatures of the computational domain were assumed to be adiabatic. The injector was located at the center of the bottom surface of the computational domain (x-y plane), and fuel spray was injected in the z-direction. The structured grid size used for calculation was uniformly distributed at 0.5 mm intervals, resulting in a corresponding grid node distribution of $217 \times 217 \times 217$, yielding over 10×10^6 hexahedral cells. Such a mesh was fine enough to accurately capture small-scale turbulence and ensure grid-independent simulation results. A calculation time step of 6×10^{-8} s was used to properly resolve the unsteady motion of high-speed and high-pressure spray evaporation. The rest of the physical sub-models were chosen consistently with the numerical framework.

Figure 23 illustrates an overview of spray and evaporation dynamics. Over an interval of 0–1.5 ms, n-dodecane droplets were injected into the combustion chamber, being rapidly atomized and evaporated. As time passed, the kerosene vapor penetrated downstream. Here, we define the distance from the injector to the furthest position in the axial direction when the mass fraction of fuel vapor
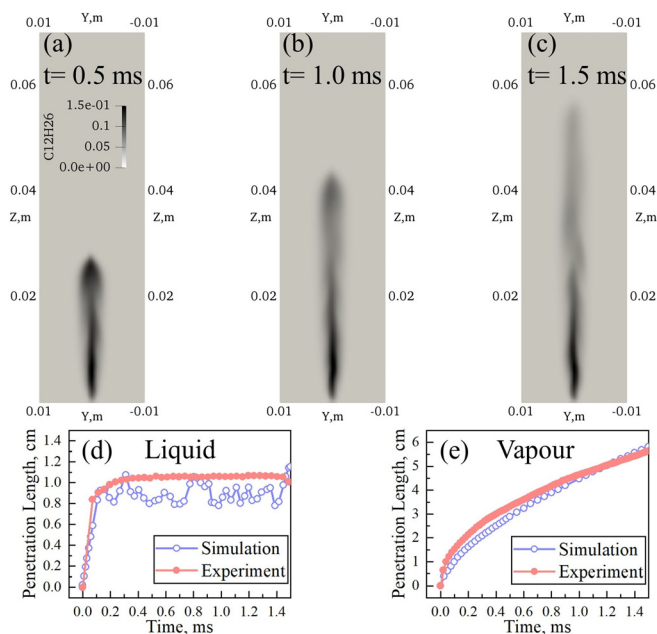

FIG. 23. Kerosene vapor contours at different instantaneous snapshots: (a) 0.5, (b) 1.0, and (c) 1.5 ms. Comparison of liquid penetration length (d) and vapor penetration length (e) with experimental measurements at intervals from 0 to 1.5 ms.

is 0.1% as the penetration length of the vapor. The penetration length of the droplet is the axial farthest distance from the injector when the mass fraction of liquid fuel is 95%. We quantitatively compared the difference between the vapor penetration length/liquid penetration length and the experimental measurements. The numerical simulation results are in very good agreement with the computational results, which verifies the validity of the Euler–Lagrange framework adopted in this paper.

2. Benchmark: Self-excited thermoacoustic instability

The second numerical validation case used in this paper is based on a single-element coaxial liquid rocket engine designed at Purdue University burning hydrogen peroxide and kerosene at critical pressure.[55] Detailed geometrical configurations, computational conditions, etc., of this engine can be found in our previous papers.[41] Here, only a brief description is given. The configuration was a combustion chamber combined with a coaxial injector with a gas-centered and liquid kerosene-swirled, in which hydrogen peroxide was dissociated at a high temperature (1030 K) with a mass concentration of 90% acting as an oxidizer. The operating pressure was 2.38 MPa, which is the critical pressure of fuel. Spontaneous thermoacoustic instability of this configuration was observed in the experiments when the length of the combustion chamber of this configuration was 38.1 cm along with the length of the oxidizer post of 17 cm.

Smith et al.[55] numerically simulated this condition based on a two-dimensional axisymmetric LES algorithm, where they used the ideal gas assumption ignoring the atomization as well as evaporation processes of liquid kerosene under critical conditions. They explained that the ideal gas assumption is valid due to the high oxidizer inlet temperature, which leads to a fast evaporation process of kerosene under critical conditions. Here, we followed their work and also employed two-dimensional axisymmetric calculations combined with the ideal gas assumption to calibrate the chemical reaction mechanism of kerosene used in this paper, as well as its ability to simulate thermoacoustic instability effects. In our previous discussion,[41] we analyzed the effect of n-dodecane vapor temperature on the simulation results due to the assumption that the kerosene vapor temperature is unknown based on the ideal gas assumption. The critical temperature and critical pressure of n-dodecane are 658 K and 1.8 MPa, respectively. Therefore, three vapor temperatures of 600, 800, and 1030 K, were used. Here, we further add the results when the kerosene vapor was 700 K, since it is only slightly higher than the critical temperature.

Figure 24 illustrates an overview of pressure dynamics in the LES results. Obvious thermoacoustic instability is observed in the pressure traces. This is evidenced by (i) high-amplitude pressure oscillations, (ii) sharp peaks in the FFT results, and (iii) a single-loop structure in the phase space trajectory. In Table VI, we quantitatively compare the errors in the dominant frequency/amplitude of the oscillations with the experimental measurements. The results show that the dominant frequency displays a relatively small difference, demonstrating the excellent simulation capability of this numerical framework for the acoustic properties inside the combustion chamber. However, there is still some error in the amplitude, which can be attributed to both the error introduced by the axisymmetric calculation and the ideal gas assumption of liquid kerosene.
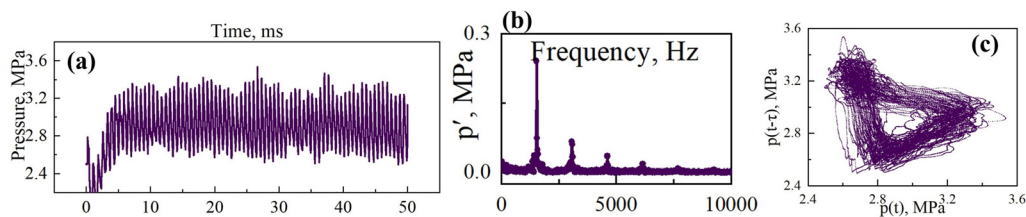
FIG. 24. (a) Time series of pressure monitored near the head of combustion chamber, (b) FFT results and (c) phase diagram. The monitoring points were set up at the same locations as the experimental measurements.

TABLE VI. Dominant frequency and amplitude of pressure traces monitored near the wall of the head of combustion chamber.

	Experiment[55]	Simulation	Error
Frequency (Hz)	1502	1533.1	2.06%
Amplitude (kPa)	297	241	18.8%

Nevertheless, these errors are not the main concern of this validation case. Therefore, the numerical framework used in this paper can be properly modeled for spray combustion of kerosene as well as thermoacoustic instability.

REFERENCES

[1]K. Manoj, S. A. Pawar, J. Kurths, and R. I. Sujith, "Rijke tube: A nonlinear oscillator," Chaos **32**(7), 072101 (2022).

[2]R. I. Sujith and V. R. Unni, "Complex system approach to investigate and mitigate thermoacoustic instability in turbulent combustors," Phys. Fluids **32**(6), 061401 (2020).

[3]M. P. Juniper and R. I. Sujith, "Sensitivity and nonlinearity of thermoacoustic oscillations," Annu. Rev. Fluid Mech. **50**, 661–689 (2018).

[4]J. O'Connor, V. Acharya, and T. Lieuwen, "Transverse combustion instabilities: Acoustic, fluid mechanic, and flame processes," Prog. Energy Combust. Sci. **49**, 1–39 (2015).

[5]W. A. Sirignano, "Driving mechanisms for combustion instability," Combust. Sci. Technol. **187**(1–2), 162–205 (2014).

[6]C. O. Paschereit, E. Gutmark, and W. Weisenstein, "Coherent structures in swirling flows and their role in acoustic combustion control," Phys. Fluids **11**(9), 2667–2678 (1999).

[7]J. O'Connor and T. Lieuwen, "Recirculation zone dynamics of a transversely excited swirl flow and flame," Phys. Fluids **24**(7), 075107 (2012).

[8]M. Gonzalez-Flesca, T. Schmitt, S. Ducruix, and S. Candel, "Large eddy simulations of a transcritical round jet submitted to transverse acoustic modulation," Phys. Fluids **28**(5), 055106 (2016).

[9]T. Poinsot, "Prediction and control of combustion instabilities in real engines," Proc. Combust. Inst. **36**(1), 1–28 (2017).

[10]L. Rayleigh and N. H. Nachtrieb, "The theory of sound," Phys. Today **10**(1), 32–34 (1957).

[11]J. C. Oefelin and V. Yang, "Comprehensive review of liquid-propellant combustion instabilities in F-1 engines," J. Propul. Power **9**(5), 657–677 (1993).

[12]P. P. Popov, A. Sideris, and W. A. Sirignano, "Triggering and restabilization of combustion instability with rocket motor acceleration," AIAA J. **54**(4), 1386–1393 (2016).

[13]L. Zhang, X. Wang, Y. Li, S.-T. Yeh, and V. Yang, "Supercritical fluid flow dynamics and mixing in gas-centered liquid-swirl coaxial injectors," Phys. Fluids **30**(7), 075106 (2018).

[14]S. Shima, K. Nakamura, and H. Gotoda, "Formation mechanism of high-frequency combustion oscillations in a model rocket engine combustor," Phys. Fluids **33**(7), 064108 (2021).

[15]J. S. Hardi, T. Traudt, C. Bombardieri, M. Boerner, S. K. Beinke, W. Armbruster, P. N. Blanco, F. Tonti, D. Suslov, B. Dally, and M. Oschwald, "Combustion dynamics in cryogenic rocket engines: Research programme at DLR Lampoldshausen," Acta Astronaut. **147**, 251–258 (2018).

[16]Y. Yu, S. Koeglmeier, J. Sisco, and W. Anderson, "Combustion instability of gaseous fuels in a continuously variable resonance chamber (CVRC)," in 44th AIAA/ASME/SAE/ASEE Joint Propulsion Conference & Exhibit (2008).

[17]J. S. Hardi, H. C. G. Martinez, M. Oschwald, and B. B. Dally, "LOx jet atomization under transverse acoustic oscillations," J. Propul. Power **30**(2), 337–349 (2014).

[18]J. S. Hardi, S. K. Beinke, M. Oschwald, and B. B. Dally, "Coupling of cryogenic oxygen–hydrogen flames to longitudinal and transverse acoustic instabilities," J. Propul. Power **30**(4), 991–1004 (2014).

[19]W. Armbruster, J. Hardi, and M. Oschwald, "Impact of shear-coaxial injector hydrodynamics on high-frequency combustion instabilities in a representative cryogenic rocket engine," Int. J. Spray Combust. Dyn. **14**(1–2), 118–130 (2022).

[20]W. Armbruster, J. S. Hardi, and M. Oschwald, "Flame-acoustic response measurements in a high-pressure, 42-injector, cryogenic rocket thrust chamber," Proc. Combust. Inst. **38**(4), 5963–5970 (2021).

[21]S. Gröning, J. S. Hardi, D. Suslov, and M. Oschwald, "Injector-driven combustion instabilities in a hydrogen/oxygen rocket combustor," J. Propul. Power **32**(3), 560–573 (2016).

[22]G. M. R. Tamanampudi, S. Sardeshmukh, W. Anderson, and C. Huang, "Combustion instability modeling using multi-mode flame transfer functions and a nonlinear Euler solver," Int. J. Spray Combust. Dyn. **12**(1), 175682772095032 (2020).

[23]C. J. Morgan, K. J. Shipley, and W. E. Anderson, "Comparative evaluation between experiment and simulation for a transverse instability," J. Propul. Power **31**(6), 1696–1706 (2015).

[24]K. Miller, J. Sisco, N. Nugent, and W. Anderson, "Experimental study of combustion instabilities in a single-element coaxial swirl injector," in 41st AIAA/ASME/SAE/ASEE Joint Propulsion Conference & Exhibit (2005).

[25]A. Urbano, L. Selle, G. Staffelbach, B. Cuenot, T. Schmitt, S. Ducruix, and S. Candel, "Exploration of combustion instability triggering using large eddy simulation of a multiple injector liquid rocket engine," Combust. Flame **169**, 129–140 (2016).

[26]K. Guo, Y. Ren, Y. Tong, W. Lin, and W. Nie, "Analysis of self-excited transverse combustion instability in a rectangular model rocket combustor," Phys. Fluids **34**(4), 047104 (2022).

[27]M. E. Harvazinski, C. Huang, V. Sankaran, T. W. Feldman, W. E. Anderson, C. L. Merkle, and D. G. Talley, "Coupling between hydrodynamics, acoustics, and heat release in a self-excited unstable combustor," Phys. Fluids **27**(4), 045102 (2015).

[28]T. M. Nguyen and W. A. Sirignano, "The impacts of three flamelet burning regimes in nonlinear combustion dynamics," Combust. Flame **195**, 170–182 (2018).

[29]T. M. Nguyen and W. A. Sirignano, "Spontaneous and triggered longitudinal combustion instability in a single-injector liquid-rocket combustor," AIAA J. **57**(12), 5351–5364 (2019).

[30]L. Kabiraj, R. I. Sujith, and P. Wahi, "Bifurcations of self-excited ducted laminar premixed flames," J. Eng. Gas Turbines Power **134**, 031502 (2012).

[31]L. Kabiraj and R. I. Sujith, "Nonlinear self-excited thermoacoustic oscillations: Intermittency and flame blowout," J. Fluid Mech. **713**, 376–397 (2012).

[32]L. Kabiraj, A. Saurabh, P. Wahi, and R. I. Sujith, "Route to chaos for combustion instability in ducted laminar premixed flames," Chaos **22**(2), 023129 (2012).

[33]Y. Guan, P. Liu, B. Jin, V. Gupta, and L. K. B. Li, "Nonlinear time-series analysis of thermoacoustic oscillations in a solid rocket motor," Exp. Therm. Fluid Sci. **98**, 217–226 (2018).

[34]C. Aoki, H. Gotoda, S. Yoshida, and S. Tachibana, "Dynamic behavior of intermittent combustion oscillations in a model rocket engine combustor," J. Appl. Phys. **127**(22), 224903 (2020).

[35]P. Kasthuri, I. Pavithran, S. A. Pawar, R. I. Sujith, R. Gejji, and W. Anderson, "Dynamical systems approach to study thermoacoustic transitions in a liquid rocket combustor," Chaos **29**(10), 103115 (2019).

[36]V. R. Unni and R. I. Sujith, "Flame dynamics during intermittency in a turbulent combustor," Proc. Combust. Inst. **36**(3), 3791–3798 (2017).

[37]C. P. Premchand, N. B. George, M. Raghunathan, V. R. Unni, R. I. Sujith, and V. Nai, "Lagrangian analysis of intermittent sound sources in the flow-field of a bluff-body stabilized combustor," Phys. Fluids **31**, 025115 (2019).

[38]T. Hashimoto, H. Shibuya, H. Gotoda, Y. Ohmichi, and S. Matsuyama, "Spatiotemporal dynamics and early detection of thermoacoustic combustion instability in a model rocket combustor," Phys. Rev. E **99**(3), 032208 (2019).

[39]P. Kasthuri, A. Krishnan, R. Gejji, W. Anderson, N. Marwan, and R. I. Sujith, "Investigation into the coherence of flame intensity oscillations in a model multi-element rocket combustor using complex networks," Phys. Fluids **34**, 034107 (2022).

[40]P. Kasthuri, S. A. Pawar, R. Gejji, W. Anderson, and R. I. Sujith, "Coupled interaction between acoustics and unsteady flame dynamics during the transition to thermoacoustic instability in a multi-element rocket combustor," Combust. Flame **240**, 112047 (2022).

[41]Y. Liu, P. Liu, Z. Wang, W. Ao, and Y. Guan, "Large eddy simulation of combustion instability in a subcritical hydrogen peroxide/kerosene liquid rocket engine: Intermittency route to period-2 thermoacoustic instability," Phys. Fluids **35**(6), 065145 (2023).

[42]F. E. C. Culick and V. Yang, *Overview of Combustion Instabilities in Liquid-Propellant Rocket Engines* (American Institute of Aeonautics & Astrophysics, 1995).

[43]W. Armbruster, J. S. Hardi, Y. Miene, D. Suslov, and M. Oschwald, "Damping device to reduce the risk of injection-coupled combustion instabilities in liquid propellant rocket engines," Acta Astronaut. **169**, 170–179 (2020).

[44]B. Emerson, J. O'Connor, M. Juniper, and T. Lieuwen, "Density ratio effects on reacting bluff-body flow field characteristics," J. Fluid Mech. **706**, 219–250 (2012).

[45]R. Smith, M. Ellis, G. Xia, V. Sankaran, W. Anderson, and C. L. Merkle, "Computational investigation of acoustics and instabilities in a longitudinal-mode rocket combustor," AIAA J. **46**(11), 2659–2673 (2008).

[46]Y. Liu, P. Liu, Z. Wang, W. Ao, G. Xu, and Y. Guan, "Numerical investigation of combustion instability in a liquid rocket engine: Interaction effect between hydrodynamics and acoustic mode," Aerosp. Sci. Technol. **143**, 108711 (2023).

[47]F. Chen, C. Ruan, T. Yu, W. Cai, Y. Mao, and X. Lu, "Effects of fuel variation and inlet air temperature on combustion stability in a gas turbine model combustor," Aerosp. Sci. Technol. **92**, 126–138 (2019).

[48]R. R. Erickson and M. C. Soteriou, "The influence of reactant temperature on the dynamics of bluff body stabilized premixed flames," Combust. Flame **158**(12), 2441–2457 (2011).

[49]Y. Liu, P. Liu, Z. Wang, W. Ao, and Y. Guan, "Numerical investigation of combustion instability in a single-element liquid rocket engine: Intermittency routes before and after thermoacoustic instability," Aerosp. Sci. Technol. **143**, 108691 (2023).

[50]C.-W. Tsang, M. F. Trujillo, and C. J. Rutland, "Large-eddy simulation of shear flows and high-speed vaporizing liquid fuel sprays," Comput. Fluids **105**, 262–279 (2014).

[51]Y. Yalcinkaya and A. G. Gungor, "Pressure gradient effect on flame-vortex interaction in lean premixed bluff-body stabilized flames," Phys. Fluids **35**, 045105 (2023).

[52]J. Li, Y. Xia, A. S. Morgans, and X. Han, "Numerical prediction of combustion instability limit cycle oscillations for a combustor with a long flame," Combust. Flame **185**, 28–43 (2017).

[53]X. Han, J. Li, and A. S. Morgans, "Prediction of combustion instability limit cycle oscillations by combining flame describing function simulations with a thermoacoustic network model," Combust. Flame **162**(10), 3632–3647 (2015).

[54]Z.-F. Zhou, G.-Y. Lu, and B. Chen, "Numerical study on the spray and thermal characteristics of R404A flashing spray using OpenFOAM," Int. J. Heat Mass Transfer **117**, 1312–1321 (2018).

[55]R. Smith, G. Xia, W. A. Anderson, and C. L. Merkle, "Computational simulations of the effect of backstep height on nonpremixed combustion instability," AIAA J. **48**(9), 1857–1868 (2010).

[56]K. C. Schadow, E. Gutmark, T. P. Parr, D. M. Parr, K. J. Wilson, and J. E. Crump, "Large-scale coherent structures as drivers of combustion instability," Combust. Sci. Technol. **64**(4–6), 167–186 (1989).

[57]K. C. Schadow and E. Gutmark, "Combustion instability related to vortex shedding in dump combustors and their passive control," Prog. Energy Combust. Sci. **18**(2), 117–132 (1992).

[58]D. Huang, J. Xu, R. Chen, and H. Meng, "Large eddy simulations of turbulent combustion of kerosene-air in a dual swirl gas turbine model combustor at high pressures," Fuel **282**, 118820 (2020).

[59]A. W. Vreman, "An eddy-viscosity subgrid-scale model for turbulent shear flow: Algebraic theory and applications," Phys. Fluids **16**(10), 3670 (2004).

[60]S. Iavarone, A. Péquin, Z. X. Chen, N. A. K. Doan, N. Swaminathan, and A. Parente, "An a priori assessment of the Partially Stirred Reactor (PaSR) model for MILD combustion," Proc. Combust. Inst. **38**(4), 5403–5414 (2021).

[61]C. Gong, M. Jangi, and X.-S. Bai, "Large eddy simulation of n-Dodecane spray combustion in a high pressure combustion vessel," Appl. Energy **136**, 373–381 (2014).

[62]K. Guo, B. Xu, Y. Ren, Y. Tong, and W. Nie, "Analysis of tangential combustion instability modes in a LO_X/kerosene liquid rocket engine based on OpenFOAM," Front. Energy Res. **9**, 810439 (2022).

[63]J. Xiong, H. Morgan, J. Krieg, F. Liu, and W. A. Sirignano, "Nonlinear combustion instability in a multi-injector rocket engine," AIAA J. **58**(1), 219–235 (2020).

[64]N. Kim, K. Jung, and Y. Kim, "Multi-environment PDF modeling for n-dodecane spray combustion processes using tabulated chemistry," Combust. Flame **192**, 205–220 (2018).

[65]Y. Guan, V. Gupta, and L. K. B. Li, "Intermittency route to self-excited chaotic thermoacoustic oscillations," J. Fluid Mech. **894**, R3 (2020).

[66]Y. Guan, K. Moon, K. T. Kim, and L. K. B. Li, "Synchronization and chimeras in a network of four ring-coupled thermoacoustic oscillators," J. Fluid Mech. **938**, A5 (2022).

[67]Y. Liu, P. Liu, Z. Wang, G. Xu, and B. Jin, "Numerical investigation of mode competition and cooperation on the combustion instability in a non-premixed combustor," Acta Astronaut. **198**, 271–285 (2022).

[68]P. E. Hamlington, A. Y. Poludnenko, and E. S. Oran, "Interactions between turbulence and flames in premixed reacting flows," Phys. Fluids **23**, 125111 (2011).

[69]J. O. Sinibaldi, C. J. Mueller, A. E. Tulkki, and J. F. Driscoll, "Suppression of flame wrinkling by buoyancy: The baroclinic stabilization mechanism," AIAA J. **36**(8), 1432–1438 (1998).

09 January 2025 08:14:45